PB83-232017

Model of Sulfate Aerosol Dynamics in Atmospheric Plumes (Journal Version)

Systems Applications, Inc., San Rafael, CA

Prepared for

Environmental Protection Agency
Research Triangle Park, NC

1982

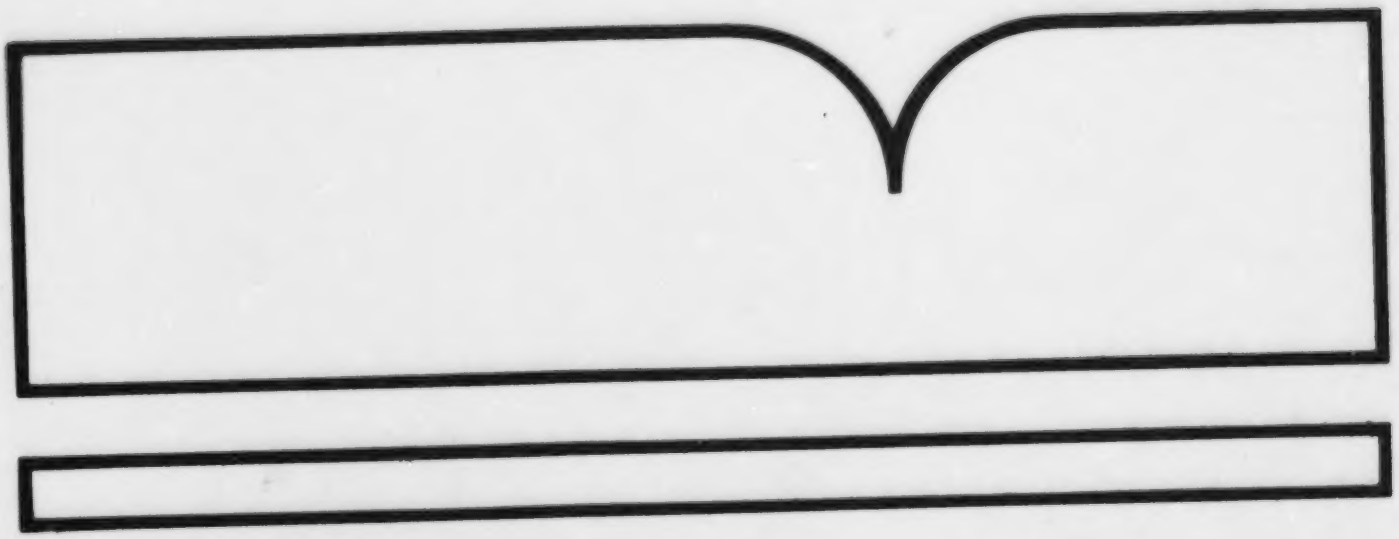

U.S. Department of Commerce
National Technical Information Service
NTIS

TECHNICAL REPORT DATA
(Please read Instructions on the reverse before completing)

1. REPORT NO. EPA-600/J-82-340	2.	3. PB83-232017
4. TITLE AND SUBTITLE A MODEL OF SULFATE AEROSOL DYNAMICS IN ATMOSPHERIC PLUMES (Journal Version)		5. REPORT DATE 1982 6. PERFORMING ORGANIZATION CODE
7. AUTHOR(S) Christian Seigneur		8. PERFORMING ORGANIZATION REPORT NO.
9. PERFORMING ORGANIZATION NAME AND ADDRESS Systems Application, Inc. 101 Lucas Valley Road San Rafael, CA 94903		10. PROGRAM ELEMENT NO. CDTA1D/11-0543 (FY-83) 11. CONTRACT/GRANT NO.
12. SPONSORING AGENCY NAME AND ADDRESS Environmental Sciences Research Laboratory - RTP, NC Office of Research and Development U.S. Environmental Protection Agency Research Triangle Park, N.C. 27711		13. TYPE OF REPORT AND PERIOD COVERED 14. SPONSORING AGENCY CODE EPA/600/09

15. SUPPLEMENTARY NOTES
REF: Atmospheric Environment Vol. 16, No. 9, pp 2207-2228, 1982

16. ABSTRACT

The evolution of atmospheric aerosols is currently a subject of concern because of its relationship to environmental issues. Recently, a rigorous approach for modeling the dynamics of a sectional aerosol distribution has been developed by Gelbard, Tambour and Seinfeld (1980) J. Colloid Interface Sci. 76, 541-556. This paper makes use of this approach and extends it through the presentation of a mathematical model that describes advective transport, turbulent diffusion, gas-phase chemistry and aerosol dynamics in atmospheric plumes. This mathematical model incorporates the Reactive Plume Model, which is a Lagrangian model used to describe plume dynamics consisting of six contiguous cells that expand as the plume is dispersed by atmospheric turbulence. It assumes a Gaussian distribution of the plume and takes into account interactions with the ambient air. The mathematical model also incorporates the Carbon-Bond Mechanism to model the gas-phase chemistry, which involves 73 reactions among 36 chemical species.

The aerosol population distribution for this model is represented by means of seven sections that have a particle diameter range of 0.01-2.15 μm. Equations describing aerosol dynamics are derived from the classical General Dynamic Equation (CDE) for a sectional aerosol distribution.

17. KEY WORDS AND DOCUMENT ANALYSIS

a. DESCRIPTORS	b. IDENTIFIERS/OPEN ENDED TERMS	c. COSATI Field/Group

18. DISTRIBUTION STATEMENT RELEASE TO PUBLIC	19. SECURITY CLASS (This Report) UNCLASSIFIED 20. SECURITY CLASS (This page) UNCLASSIFIED	21. NO. OF PAGES 23 22. PRICE

EPA Form 2220-1 (Rev. 4-77) PREVIOUS EDITION IS OBSOLETE

REPRODUCED BY
NATIONAL TECHNICAL
INFORMATION SERVICE
U.S. DEPARTMENT OF COMMERCE
SPRINGFIELD, VA. 22161

U.S. Government is authorized to reproduce and sell this report. Permission for further reproduction must be obtained from the copyright owner.

Atmospheric Environment Vol. 16, No. 9, pp. 2207–2228, 1982
Printed in Great Britain.

0004-6981/82/092207-22 $03.00/0
© 1982 Pergamon Press Ltd.

EPA-600/J-82-340
JOURNAL ARTICLE

A MODEL OF SULFATE AEROSOL DYNAMICS IN ATMOSPHERIC PLUMES

CHRISTIAN SEIGNEUR
Systems Applications, Inc., 101 Lucas Valley Road, San Rafael, CA 94903, U.S.A.

(*First received* 6 *November* 1980 *and in final form* 3 *November* 1981)

Abstract—The evolution of atmospheric aerosols is currently a subject of concern because of its relationship to environmental issues. Recently, a rigorous approach for modeling the dynamics of a sectional aerosol distribution has been developed by Gelbard, Tambour and Seinfeld (1980) *J. Colloid Interface Sci.* **76**, 541–556. This paper makes use of this approach and extends it through the presentation of a mathematical model that describes advective transport, turbulent diffusion, gas-phase chemistry and aerosol dynamics in atmospheric plumes. This mathematical model incorporates the Reactive Plume Model, which is a Lagrangian model used to describe plume dynamics consisting of six contiguous cells that expand as the plume is dispersed by atmospheric turbulence. It assumes a Gaussian distribution of the plume and takes into account interactions with the ambient air. The mathematical model also incorporates the Carbon-Bond Mechanism to model the gas-phase chemistry, which involves 73 reactions among 36 chemical species.

The aerosol population distribution for this model is represented by means of seven sections that have a particle diameter range of 0.01–2.15 μm. Equations describing aerosol dynamics are derived from the classical General Dynamic Equation (GDE) for a sectional aerosol distribution. The dynamic processes described in the model include inter- and intra-sectional coagulation, condensation of acid sulfate or ammonium sulfate and heterogeneous oxidation of sulfur dioxide (SO_2) in each section, as well as new-particle formation in the lowest section. Condensation is diffusion-limited and new-particle formation is estimated from monomer balance theory. Heterogeneous oxidation of SO_2 in the aerosol phase is parameterized by means of a pseudo-first-order chemical reaction.

The aerosol dynamics module is evaluated with smog chamber data obtained for an aerosol-H_2SO_4-H_2O system. Aerosol plume model predictions are compared with airborne measurements obtained from the plume of the Navajo power plant on four different days during the VISTTA program, at downwind distances ranging from 25 to 88 km. Important characteristics of aerosol dynamics are well described by the model. Secondary aerosol formation is most apparent in the 0.01–0.1 μm size range. Maximum predicted SO_2 homogeneous oxidation rates are 0.5 and 0.6%h^{-1} for the summer and winter cases, respectively. Sensitivity studies performed with the aerosol plume model showed that background hydrocarbon concentrations, relative humidity and photolysis rates affect secondary aerosol formation most, whereas atmospheric stability has little effect.

1. INTRODUCTION

The formation and growth of aerosols in the atmosphere has been a subject of growing concern in recent years because environmental issues such as atmospheric visibility, acid rain and the health effects of fine particulate matter are related to the concentration, chemical composition and size distribution of these airborne particles. To understand and predict the chemical and physical processes that govern the evolution of atmospheric aerosols, mathematical models of aerosol dynamics must be developed.

The dynamic behavior of an aerosol population that undergoes coagulation, condensation and nucleation processes can be described by a partial integro-differential equation, the so-called General Dynamic Equation (GDE). The numerical solution of the GDE has been obtained by means of collocation on finite elements for a continuous (Middleton and Kiang, 1978) and a discrete-continuous (Gelbard and Seinfeld, 1979) representation of the aerosol population. Computationally, such methods are relatively expensive and this prevents their inclusion in air quality models that must also describe atmospheric transport, dispersion and chemistry.

Simpler models of the aerosol population evolution have been developed to describe aerosol dynamics in the atmosphere. In some atmospheric models, coagulation processes have been neglected, allowing the GDE to be solved more easily since numerical difficulties in its solution arise from the coagulation term. Such models have been developed and applied on urban and regional scales (Chu and Seinfeld, 1975; Peterson and Seinfeld, 1977) when aerosol concentrations are low enough to allow coagulation to be neglected. However, this hypothesis cannot, in general, be applied to atmospheric plumes in which coagulation is a major part of the evolution of aerosol distributions.

Considerations of aerosol dynamics, atmospheric processes and possibly Greek mythology led to he development and naming of the Phoenix model (Eltgroth and Hobbs, 1979), which provides a good representation of the physical and chemical processes that govern aerosol dynamics in atmospheric plumes. The Phoenix model includes advection, turbulent diffusion, gas-phase chemistry, coagulation and sedi-

mentation of aerosols, as well as gas-to-particle conversion. Aerosol population distributions for the Phoenix model are represented by three log-normal distributions. This approximation allows the use of a simpler form of the GDE.

Another approach to modeling aerosol dynamics uses a sectional representation of the aerosol population to consider transport, turbulent diffusion, coagulation and sedimentation of six particle sizes (from 0.001 to 100 μm) (Sheih, 1977). However, the representation of the aerosol population by six sizes is an approximation difficult to evaluate.

A more rigorous approach to the sectional representation of an aerosol distribution has recently been developed (Gelbard *et al.*, 1980) for coagulation, and evaluated for the number and volume distribution of an aerosol population against the accurate solution of the GDE mentioned previously (Gelbard and Seinfeld, 1979). This approach, which has the advantage of being both mathematically and physically sound, is used in the mathematical model presented here. The single approximation made with this approach is the sectionalization of the aerosol size distribution, and it should be noted that when the section size decreases, the solution tends towards the solution of the classical GDE. Recently, the sectional equations for volume distribution have been extended to include condensation and chemical reaction in the aerosol phase (Gelbard and Seinfeld, 1980; Basset *et al.*, 1981).

In this paper, we consider the solution of the GDE for the volume distribution on the basis of this sectional approach. The physical processes considered in the model include inter- and intrasectional coagulation, gas-to-particle conversion, first-order chemical reaction in the aerosol phase and removal processes. An important feature of this model is the treatment of gas-to-particle conversion, which describes condensation on pre-existing aerosols as well as new aerosol formation. The relative rates of condensation and new aerosol formation are determined from the rate of formation of the condensing species and the total aerosol surface area according to monomer balance theory (McMurry, 1980). New aerosols are thus allowed to coagulate between themselves and with the sectional aerosol populations. The aerosol model is cast in a scheme similar to that of a chemical mechanism so that it can be included easily in air quality models that already contain a chemistry module. Model predictions are compared with data from a smog chamber experiment.

The aerosol model is then incorporated into a plume model that includes advective transport, turbulent diffusion, gas-phase chemistry and surface deposition. This model is used to simulate the evolution of aerosols and chemical species concentrations in the plume of the Navajo generating station near Page, Arizona and the model results are compared with experimental results obtained during the VISTTA program. Finally, several sensitivity studies are carried out to evaluate the effect of SO_2 and NO_x emission rates, relative humidity, SO_2 heterogeneous oxidation, background hydrocarbon concentration, atmospheric stability and photolysis rates on the formation of secondary aerosols in an atmospheric plume.

2. THE MODELING OF AEROSOL DYNAMICS

2.1. *Description of the aerosol model*

In the sectional approach to the simulation of aerosol dynamics, the particle size domain is divided into sections and some function of the aerosol concentration is considered to be constant within each section. The sectional GDE can be solved for any aerosol distribution function (e.g. number, surface or volume distribution). To satisfy the condition of mass conservation, the aerosol volume concentration is chosen here as the conserved quantity in the sectional model.

The aerosol particle size range considered in this model extends from 0.01 to 2.15 μm in diameter. The lowest size corresponds approximately to the minimum detectable particle size. The upper particle diameter corresponds to the upper limit of the accumulation mode. Number concentrations above 2 μm are usually low enough (e.g. Hobbs *et al.*, 1979; Whitby *et al.*, 1972; Whitby *et al.*, 1975) so that the coarse mode does not greatly affect aerosol dynamics in the nuclei and accumulation range. When number concentrations in the coarse mode are high enough that aerosols from the nuclei mode preferentially coagulate with coarse-mode aerosols rather than with aerosols from the accumulation mode, additional sections with particle diameters above 2 μm can easily be introduced into the model.

The particle size domain is divided into m sections of equal size $(x_l - x_{l-1})$; $l = 1, \ldots, m$, where $x = \log(d_p)$ and d_p is the particle diameter.

The following integral quantity is defined for each section l:

$$Q_l(t) = \int_{x_{l-1}}^{x_l} \bar{q}_l(t)\,\mathrm{d}x, \quad l = 1, \ldots, m, \tag{1}$$

where $\bar{q}_l(t)$ is the continuous volume distribution function that is assumed to be constant in section l. If $Q_x(t)$ is the total particle volume,

$$\bar{q}_l(t) = \frac{\mathrm{d}Q_x(t)}{\mathrm{d}\log d_p}, \quad x_{l-1} < \log d_p \leqslant x_l. \tag{2}$$

Since $\bar{q}_l(t)$ is assumed to be constant within each section, the integral quantity, $Q_l(t)$, is given by (3):

$$Q_l(t) = \bar{q}_l(t)\,(x_l - x_{l-1}). \tag{3}$$

Therefore, the volume distribution is represented by a step function with values, $\bar{q}_l(t)$, over each section, $l = 1, \ldots, m$.

The sectional equations that govern the dynamics of

aerosol formation in this model are

$$\frac{dQ_l}{dt} = \sum_{i=1}^{l-1} {}^a\beta_{i,l-1} Q_i Q_{l-1} - \sum_{i=1}^{m} {}^b\beta_{i,l} Q_i Q_l + {}^a\bar{\phi}_l Q_l + {}^b\bar{\phi}_{l-1} Q_{l-1} - {}^b\bar{\phi}_l Q_l + {}^a\bar{\psi}_l Q_l + {}^b\bar{\psi}_{l-1} Q_{l-1} - {}^b\bar{\psi}_l Q_l + \delta(1) J_1 + S_l - L_l Q_l \quad l = 1, \ldots, m, \quad (4)$$

where in the equations for $l = 1, \ldots, m$, the first, fourth and seventh terms on the right-hand side are not evaluated for $l = 1$. The first term represents the formation of aerosols in section l by coagulation of aerosols from lower sections. The second term describes the coagulation of aerosols from section l with aerosols from all other sections (including section l). The third term accounts for the increase in volume in section l as a result of condensation and the fourth and fifth terms represent growth by condensation into and out of section l, respectively. The sixth, seventh and eighth terms similarly represent growth caused by aerosol phase reaction. The ninth term, where $\delta(1)$ is the Chronecher index, represents new-particle formation. The tenth term represents the rate of generation of aerosols in section l, e.g. primary particulate emission, and the last term accounts for aerosol removal, e.g. loss to the wall of a smog chamber or surface deposition.

The sectional coefficients are listed in Table 1; following paragraphs present the derivation of each of the terms of (4) and the calculation of the sectional coefficients.

Coagulation. Gelbard *et al.* (1980) derived the basic equations that govern aerosol coagulation for a sectional representation of the aerosol distribution:

$$\frac{dQ_l(t)}{dt} = \sum_{i=1}^{l-1} {}^a\bar{\beta}_{i,l-1} Q_i Q_{l-1} - \sum_{i=1}^{m} {}^b\bar{\beta}_{i,l} Q_i Q_l, \quad l = 1, \ldots, m, \quad (5)$$

where the first term on the right-hand side is not evaluated for $l = 1$. The Brownian coagulation coefficient $\beta(x, y)$, as given by the Fuchs–Philips formula (Sitarski and Seinfeld, 1977), was chosen with an accomodation coefficient of 1. It agrees well with experimental data in the transition regime and corresponds to theoretical formulas derived from kinetic theory and diffusion theory in the free-molecule range and the continuum range, respectively.

Diffusion-limited condensation. The sectional equations for gas-to-particle conversion can be expressed in the following manner:

$$\frac{dQ_l}{dt} = {}^a\bar{\phi}_l Q_l + {}^b\bar{\phi}_{l-1} Q_{l-1} - {}^b\bar{\phi}_l Q_l, \quad l = 1, \ldots, m, \quad (6)$$

where ${}^a\bar{\phi}_l$ and ${}^b\bar{\phi}_l$, $l = 1, \ldots, m$ are the sectional coefficients listed in Table 1. The derivation of this equation is described in the Appendix.

Sulfuric acid is produced in the gas phase by homogeneous oxidation of SO_2. It is assumed in the derivation of the sectional condensation coefficients that H_2SO_4 is the condensing species. It should be noted, however, that because of the use of monomer balance theory to describe gas-to-particle conversion, the model equations are not sensitive to the choice of the condensing species. Some hydrated radicals such as HSO_5-nH_2O have been suggested as possible routes for gas-to-particle conversion (Davis *et al.*, 1979); at low relative humidity, ammonium sulfate could also be the condensing species (Richards *et al.*, 1981). Formation of aerosol nitrates and organics is not considered in this model.

It is assumed that aerosol particles are either composed of a H_2SO_4 solution or of ammonium sulfate. In the first case, the mole fraction of H_2SO_4 in the aerosol phase depends on relative humidity, but does not vary notably with particle size except at high humidities (above 80% relative himidity) for small particles (below 0.1 μm) (Mirabel and Katz, 1974). When H_2SO_4 condenses on the aerosol droplet, the increase in sulfate concentration lowers the water activity. This creates a water vapor pressure gradient between the droplet surface and the bulk gas phase. Condensation of water vapor then occurs to restore the equilibrium. This process is of the order of 10^{-3} s and is very fast when compared with the diffusion-limited condensation of H_2SO_4. Thus, water vapor condensation occurs simultaneously with H_2SO_4 condensation and the amount of water vapor condensing can be determined from the aerosol composition because thermodynamic equilibrium between the gas phase and the liquid phase must be conserved. In the case of ammonium sulfate aerosol, ammonia is allowed to condense to maintain stoichiometry in the aerosol phase.

Diffusion-limited condensation of H_2SO_4 is well described by the Fuchs–Sutugin formula (Fuchs and Sutugin, 1971; Davis and Ray, 1978):

$$\phi = v' \cdot \frac{2\pi D d_p}{(1 + KnLn)} ([H_2SO_4] - [H_2SO_4]_s), \quad (7)$$

where ϕ is the rate of condensation of monomers, i.e. H_2SO_4-nH_2O or $(NH_4)_2SO_4$, $Ln = (2.66\lambda + 0.71 d_p)/(2\lambda + d_p)$, $Kn = 2\lambda/d_p$ is the Knudsen number, λ is the mean free path of the condensing species, d_p is the particle diameter, D is the diffusion coefficient of H_2SO_4 in the air and v' is the volume of a monomer. The monomer volume is defined as M/ρ, where M is the molar mass of the monomer H_2SO_4-nH_2O or

Table 1. Sectional coefficients

(a) *Coagulation coefficients*

(1) $2<l\leqslant m$; $1\leqslant i<l-1$:

$$^{a}\bar{\beta}_{i,l-1}=\int_{x_{i-1}}^{x_i}\int_{f(v_{l-1}-v)}^{x_{i-1}}\frac{(u+v)\beta(u,v)}{uv(x_i-x_{i-1})(x_{l-1}-x_{l-2})}\,dy\,dx$$

$2\leqslant l\leqslant m$; $i=l-1$:

$$^{a}\bar{\beta}_{i,l-1}=\tfrac{1}{2}\int_{x_{l-2}}^{f(v_{l-1}-v_{l-2})}\int_{f(v_{l-1}-v)}^{x_{l-1}}\frac{(u+v)\beta(u,v)}{uv(x_i-x_{i-1})(x_{l-1}-x_{l-2})}\,dy\,dx+\tfrac{1}{2}\int_{f(v_{l-1}-v_{l-2})}^{x_{l-1}}\int_{x_{l-2}}^{x_{l-1}}\frac{(u+v)\beta(u,v)}{uv(x_i-x_{i-1})(x_{l-1}-x_{l-2})}\,dy\,dx.$$

(2) $2\leqslant l\leqslant m$; $1\leqslant i<l$:

$$^{b}\bar{\beta}_{i,l}=\int_{x_{i-1}}^{x_i}\int_{f(v_l-v)}^{x_i}\frac{\beta(u,v)}{v(x_i-x_{i-1})(x_l-x_{l-1})}\,dy\,dx-\int_{x_{i-1}}^{x_i}\int_{x_{l-1}}^{f(v_l-v)}\frac{\beta(u,v)}{u(x_i-x_{i-1})(x_l-x_{l-1})}\,dy\,dx.$$

$1\leqslant l\leqslant m$; $i=l$:

$$^{b}\bar{\beta}_{i,l}=\,^{a}\bar{\beta}_{i,l}.$$

$1\leqslant l<m$; $l<i$:

$$^{b}\bar{\beta}_{i,l}=\int_{x_{i-1}}^{x_i}\int_{x_{l-1}}^{x_i}\frac{\beta(u,v)}{v(x_i-x_{i-1})(x_l-x_{l-1})}\,dy\,dx.$$

(b) *Condensation coefficients*

(1) Diffusion-limited

$1\leqslant l\leqslant m$:

$$^{a}\bar{\phi}_l=\int_{x_{l-1}}^{x_l}\frac{\phi(x)}{v(x_l-x_{l-1})}\,dx$$

$$^{b}\bar{\phi}_l=\frac{\phi(x_l)\cdot(v_l+v')}{3\ln(10)v_l^2(x_l-x_{l-1})}.$$

(2) Aerosol phase reaction

$1\leqslant l\leqslant m$:

$$^{a}\bar{\psi}_l=v'Kk_a[SO_2]$$

$$^{b}\bar{\psi}_l=\frac{v'Kk_a[SO_2](v_l+v')}{3\ln(10)v_l(x_l-x_{l-1})}.$$

(c) *Source and removal coefficients*

(1) New-particle formation

$l=1$: $\bar{J}_1=\gamma Rv'$.

(2) Primary emissions

$1\leqslant l\leqslant m$: $\bar{S}_l=\int_{x_{l-1}}^{x_l}\frac{S(x)}{x_l-x_{l-1}}\,dx.$

(3) Removal

$1\leqslant l\leqslant m$: $\bar{L}_l=\int_{x_{l-1}}^{x_l}\frac{L(x)}{x_l-x_{l-1}}\,dx.$

Note:

$x=\log(d_p)=f(v)$, $u=f^{-1}(y)$, $v=f^{-1}(x)$; $\beta(x,y)$ = Fuchs–Phillips Brownian coagulation coefficient; $\phi(x)$ = Fuchs–Sutugin growth law; v' = monomer volume; K = equilibrium constant for reacting species SO_2; k_a = pseudo-first-order rate parameter; $[SO_2]$ = gas phase concentration of SO_2; $S(x)$ = rate of primary aerosol emission; $L(x)$ = rate of aerosol removal; R = rate of production of H_2SO_4 and γ = ratio of new-particle formation rate to gas-to-particle conversion rate.

$(NH_4)_2SO_4$, and ρ is the density of the aerosol. $[H_2SO_4]$ and $[H_2SO_4]_s$ are the concentrations of H_2SO_4 in the bulk gas phase and at the surface of the aerosol droplet, respectively. Except at very low relative humidities, the equilibrium vapor pressure of H_2SO_4 is negligible (Gmitro and Vermeulen, 1969), and it can be assumed that its pressure at the aerosol surface is zero.

Condensation limited by chemical reaction in the aerosol phase. Oxidation of SO_2 occurs in the gas phase as well as in the aerosol phase. Oxidation of SO_2 into sulfate in the aerosol phase can occur through uncatalyzed reaction with O_2, O_3 and H_2O_2, or through reaction with O_2 catalyzed by iron or manganese ions. It has been shown that heterogeneous oxidation of SO_2 can account for about 20% of aerosol growth in power plant plumes (McMurry *et al.*, 1981). It is therefore important to allow for this chemical pathway in an aerosol plume model.

The growth law corresponding to aerosol phase reaction is given in (8):

$$\psi = \frac{\pi d_p^3}{6} v' k_a K [SO_2]. \tag{8}$$

where k_a is the pseudo-first-order oxidation-rate constant in min^{-1}, and K is the equilibrium constant for SO_2 between the gas phase and the liquid phase, $K = 1.24 \times 10^{-9}$ mol cm^{-3} ppm^{-1}. The simultaneous condensation of water vapor to maintain thermodynamic equilibrium as new sulfate is formed is taken into account in (8) through the term v'. The growth law resulting from droplet reaction is proportional to the droplet volume.

The sectional droplet phase-reaction coefficients depend on relative humidity through v'. Sulfur dioxide conversion from the gas phase to the aerosol phase is calculated by mass balance.

The sectional equations for aerosol growth by aerosol phase reaction are given in (9):

$$\frac{dQ_l}{dt} = {}^a\overline{\psi}_l Q_l + {}^b\overline{\psi}_{l-1} Q_{l-1} - {}^b\overline{\psi}_l Q_l,$$

$$l = 1, \ldots, m. \tag{9}$$

They are derived in the same manner as the equations for diffusion-limited condensation. The sectional coefficients, ${}^a\overline{\psi}_l$ and ${}^b\overline{\psi}_l$, are listed in Table 1. Note that since $v' \ll v_l$, and this growth law is proportional to the volume of the particle, the sectional aerosol phase-reaction coefficients are nearly constant for all sections $l = 1, \ldots, m$. These coefficients depend on relative humidity through v'. Sulfur dioxide conversion from the gas phase to the aerosol phase is calculated by mass balance.

New-particle formation. The rate of new-particle formation can be estimated from classical nucleation theory (Yue and Hamill, 1979). This approach has been used in some models of aerosol dynamics (Middleton and Kiang, 1978); however, the extrapolation to the molecular regime of bulk properties such as surface tension, and the uncertainties in the equilibrium vapor pressure of H_2SO_4, introduce uncertainties in the theory that are difficult to evaluate. Comparisons of new-particle formation rates predicted by classical nucleation theory with experimental data do not give good agreement (McMurry and Friedlander, 1979), therefore, another approach—monomer balance theory—will be considered here.

In the monomer balance theory, the rate of new-particle formation at a given particle size can be estimated from the coagulation dynamics of monomers, clusters and aerosols. This concept has been used to represent gas-to-particle conversion in the GDE (Gelbard and Seinfeld, 1979); we consider here the monomer balance theory developed by McMurry (1980), which is used to predict the rate of new-particle formation. This theory assumes that the activation energy for nucleation is negligible; in addition, re-evaporation is neglected (a good approximation if the production rate of H_2SO_4 is high enough) and a quasi-steady-state is assumed here for the ultra-fine aerosol distribution. Cluster–cluster coagulation, which was not considered in the original theory (McMurry and Friedlander, 1979) has now been included in the calculations (McMurry, 1980).

The rate of new-particle formation is evaluated from a balance between these elements: the rate of formation of sulfuric acid; condensation on existing aerosols (i.e. coagulation of monomers such as H_2SO_4–nH_2O or $(NH_4)_2SO_4$ and clusters of monomers with aerosols) and, formation of new particles at a given particle size by coagulation of monomers with clusters and clusters with clusters.

The predicted rate of new-particle formation can be related to the dimensionless parameter Ld that depends on the total surface area of existing aerosols and on the formation rate of H_2SO_4 (McMurry and Friedlander, 1979).

$$Ld = \frac{1}{16\sqrt{3}\pi}\left(\frac{4\pi}{3}\right)^{1/6} \frac{k_b T^{1/2}}{v'^{7/6}\rho^{1/2}} \frac{A^2}{R}, \tag{10}$$

where k_b is the Boltzmann's constant, T the temperature, v' the volume of a monomer, ρ the aerosol density, A the total aerosol surface area and R the rate of production of H_2SO_4. The new-particle formation rate can also depend on relative humidity because the number of monomers of H_2SO_4–nH_2O in a particle of a given size varies with humidity; however, this effect was not considered in this model.

Since the monomer balance theory has been shown to provide good estimates of the relative rates of new-particle formation and condensation when compared with data from smog chamber experiments (McMurry and Friedlander, 1979), it is used to estimate the rate of new-particle formation, J_1, in Equation (4). The fraction, γ, of monomers involved in the formation of new particles is calculated from the results of the

steady-state monomer balance theory reported by McMurry (1980) as follows. A function relating γ to the dimensionless parameter Ld was fitted to the steady-state calculations of McMurry. The parameter Ld is calculated at each time step and for each location, i.e. plume cell and background, from the values of the total aerosol surface area and rate of production of H_2SO_4 according to Equation (10). Then, the value of γ is calculated from the value of Ld. The rate of new-particle formation in section Q_1 is given by (11).

$$J_1 = \gamma R v', \tag{11}$$

where R is the rate of production of H_2SO_4, i.e. the production rate of monomers, and v' is the volume of a monomer ($H_2SO_4 \cdot nH_2O$ or $(NH_4)_2\,SO_4$). The remaining fraction $(1-\gamma)$ of monomers condenses on existing aerosols according to the diffusion law described previously.

The concentration of H_2SO_4 in the gas phase, SA, is determined by the rate of homogeneous oxidation of SO_2 and the rate of gas-to-particle conversion. The former is defined by the gas-phase chemical kinetic mechanism. The rate of gas-to-particle conversion is calculated from the sectional equations for diffusion-limited condensation and new-particle formation. The kinetic equation for gaseous H_2SO_4 is as follows:

$$\frac{d[SA]}{dt} = R - \sum_{i=1}^{m} \frac{2\pi D d_p}{(1 + KnLn)} [SA] \frac{Q_i}{\pi d_p^3/6} - \gamma R, \tag{12}$$

where the first term on the right-hand side is the rate of production of H_2SO_4 in the gas phase, the second term is the rate of condensation of H_2SO_4 on existing aerosols, and the last term represents the rate of removal of H_2SO_4 due to new particle formation. A steady-state approximation leads to the following relationship to calculate the H_2SO_4 concentration in the gas phase.

$$[SA] = \frac{(1-\gamma)R}{\sum_{i=1}^{m} 12DQ_i[(1 + KnLn)d_p^2]}. \tag{13}$$

Source and removal of aerosols. Primary emissions of aerosols can be incorporated into the model by sectionalizing the emission rates in the following manner:

$$\frac{dQ_l}{dt} = \int_{x_{l-1}}^{x_l} \frac{S(x)}{x_l - x_{l-1}}\,dx \qquad l = 1, \ldots, m. \tag{14}$$

This can be expressed in the sectional form of (4) by introducing the sectional emission coefficient $\bar{S}_l$, shown in Table 1.

Removal of aerosols occurs in a smog chamber through losses to the chamber walls (McMurry, 1977) and in the atmosphere through surface deposition (Husar *et al.*, 1978). These rate processes are proportional to the aerosol concentrations and can be described by (15):

$$\frac{dQ_l}{dt} = Q_l \int_{x_{l-1}}^{x_l} \frac{L(x)}{x_l - x_{l-1}}\,dx, \quad l = 1, \ldots, m. \tag{15}$$

The sectional removal coefficients, $\bar{L}_l$, $l = 1, \ldots, m$, which are listed in Table 1, can be defined to cast this equation in the form of (4).

2.2. *Sectional interaction scheme for aerosol dynamics*

It is convenient to cast the aerosol model into the form of a sectional interaction scheme that is similar to one of chemical reactions. This allows for the incorporation of the aerosol model into air quality models that comprise an atmospheric chemistry subroutine (e.g. photochemistry, plume, urban airshed and regional models), without any substantial modification of the air quality model's computer code.

This sectional interaction scheme is presented in Table 2 for a 7-section model. The species Q_l, $l = 1, \ldots, m$ represent the aerosol population of the sections, and their concentrations are the aerosol volume concentrations in these sections which are expressed in $\mu m^3\,cm^{-3}$. The species SA and AERS refer to H_2SO_4 in the gas phase and total sulfate in the aerosol phase, respectively; they are expressed in ppm. It should be noted that this scheme is written for computational convenience and caution is advised in considering the physical meaning of the interactions.

The scheme involves 28 inter- and intrasectional coagulation processes, 7 interactions between gaseous H_2SO_4 and aerosol sectional populations that describe diffusion-limited condensation, 7 interactions between SO_2 and aerosol sectional populations that describe growth by heterogeneous chemical reaction, and 1 interaction that describes new-particle formation.

In the coagulation interactions (1–28), aerosols from sections i and l ($i \leqslant l$) collide to produce aerosols in sections l and $l+1$:

$$Q_i + Q_l \xrightarrow{{}^{c}k_{il}} {}^{c}a_{il}\,Q_l + {}^{c}b_{il}\,Q_{l+1},$$

$$l = 1, \ldots, m, \quad i = 1, \ldots, l,$$

where ${}^{c}a_{il}$ is not evaluated for $i = l$ and ${}^{c}b_{il}$ is not evaluated for $l = m$. The coagulation rate is proportional to the aerosol population of the coagulating sections. The stoichiometric coefficients and rate parameters are calculated from the sectional coagulation coefficients by matching the kinetic equations of the coagulation interactions with Equation (5). These parameters are listed in Table 3.

Interactions (29)–(35) represent the growth by diffusion-limited condensation:

$$Q_l + SA \xrightarrow{{}^{d}k_l} {}^{d}a_l\,Q_l + {}^{d}b_l\,Q_{l+1} + {}^{d}c_l\,AERS + {}^{d}d_l\,SA,$$

$$l = 1, \ldots, m.$$

Table 2. Sectional interaction scheme of aerosol dynamics*

Interactions	Rate parameters
(1) $Q_1 + Q_1 = 2.000\,Q_2$	9.577×10^{-3}
(2) $Q_2 + Q_1 = 1.807\,Q_2 + 0.193\,Q_3$	1.514×10^{-2}
(3) $Q_2 + Q_2 = 2.000\,Q_3$	9.315×10^{-4}
(4) $Q_3 + Q_1 = 1.799\,Q_3 + 0.201\,Q_4$	3.464×10^{-3}
(5) $Q_3 + Q_2 = 1.833\,Q_3 + 0.167\,Q_4$	1.339×10^{-3}
(6) $Q_3 + Q_3 = 2.000\,Q_4$	6.582×10^{-5}
(7) $Q_4 + Q_1 = 1.805\,Q_4 + 0.195\,Q_5$	8.572×10^{-4}
(8) $Q_4 + Q_2 = 1.822\,Q_4 + 0.178\,Q_5$	2.439×10^{-4}
(9) $Q_4 + Q_3 = 1.846\,Q_4 + 0.154\,Q_5$	8.851×10^{-5}
(10) $Q_4 + Q_4 = 2.000\,Q_5$	4.163×10^{-6}
(11) $Q_5 + Q_1 = 1.812\,Q_5 + 0.188\,Q_6$	2.033×10^{-4}
(12) $Q_5 + Q_2 = 1.819\,Q_5 + 0.181\,Q_6$	5.056×10^{-5}
(13) $Q_5 + Q_3 = 1.832\,Q_5 + 0.168\,Q_6$	1.426×10^{-5}
(14) $Q_5 + Q_4 = 1.852\,Q_5 + 0.148\,Q_6$	5.512×10^{-6}
(15) $Q_5 + Q_5 = 2.000\,Q_6$	2.997×10^{-7}
(16) $Q_6 + Q_1 = 1.794\,Q_6 + 0.266\,Q_7$	4.602×10^{-5}
(17) $Q_6 + Q_2 = 1.815\,Q_6 + 0.185\,Q_7$	1.081×10^{-5}
(18) $Q_6 + Q_3 = 1.823\,Q_6 + 0.177\,Q_7$	2.740×10^{-5}
(19) $Q_6 + Q_4 = 1.836\,Q_6 + 0.164\,Q_7$	8.429×10^{-7}
(20) $Q_6 + Q_5 = 1.853\,Q_6 + 0.147\,Q_7$	8.391×10^{-7}
(21) $Q_6 + Q_6 = 2.000\,Q_7$	2.609×10^{-8}
(22) $Q_7 + Q_1 = -0.312\,Q_7$	1.017×10^{-3}
(23) $Q_7 + Q_2 = 0.160\,Q_7$	2.329×10^{-6}
(24) $Q_7 + Q_3 = 0.180\,Q_7$	5.629×10^{-7}
(25) $Q_7 + Q_4 = 0.182\,Q_7$	1.554×10^{-7}
(26) $Q_7 + Q_5 = 0.184\,Q_7$	5.917×10^{-8}
(27) $Q_7 + Q_6 = 0.184\,Q_7$	3.459×10^{-8}
(28) $Q_7 + Q_7$	2.44×10^{-9}
(29) $Q_1 + SA = 1.559\,Q_1 + 0.2203\,Q_2 + 5.9 \times 10^{-5}\,AERS + 9.9994 \times 10^{-1}\,SA$	2.814×10^{4}
(30) $Q_2 + SA = 1.572\,Q_2 + 0.2138\,Q_3 + 6.0 \times 10^{-5}\,AERS + 9.9994 \times 10^{-1}\,SA$	1.225×10^{4}
(31) $Q_3 + SA = 1.594\,Q_3 + 0.2028\,Q_4 + 6.1 \times 10^{-5}\,AERS + 9.9994 \times 10^{-1}\,SA$	4.914×10^{3}
(32) $Q_4 + SA = 1.627\,Q_4 + 0.1863\,Q_5 + 6.2 \times 10^{-5}\,AERS + 9.9994 \times 10^{-1}\,SA$	1.705×10^{3}
(33) $Q_5 + SA = 1.658\,Q_5 + 0.1706\,Q_6 + 6.3 \times 10^{-5}\,AERS + 9.9994 \times 10^{-1}\,SA$	4.954×10^{2}
(34) $Q_6 + SA = 1.674\,Q_6 + 0.1627\,Q_7 + 6.4 \times 10^{-5}\,AERS + 9.9994 \times 10^{-1}\,SA$	1.249×10^{2}
(35) $Q_7 + SA = 1.683\,Q_7 + 6.4 \times 10^{-5}\,AERS + 9.9994 \times 10^{-1}\,SA$	2.901×10^{1}
(36) $Q_1 + SO_2 = 1.400\,Q_1 + 0.3000\,Q_2 + 5.3 \times 10^{-5}\,AERS + 9.9995 \times 10^{-1}\,SO_2$	2.000×10^{-2}
(37) $Q_2 + SO_2 = 1.400\,Q_2 + 0.3000\,Q_3 + 5.3 \times 10^{-5}\,AERS + 9.9995 \times 10^{-1}\,SO_2$	2.000×10^{-2}
(38) $Q_3 + SO_2 = 1.400\,Q_3 + 0.3000\,Q_4 + 5.3 \times 10^{-5}\,AERS + 9.9995 \times 10^{-1}\,SO_2$	2.000×10^{-2}
(39) $Q_4 + SO_2 = 1.400\,Q_4 + 0.3000\,Q_5 + 5.3 \times 10^{-5}\,AERS + 9.9995 \times 10^{-1}\,SO_2$	2.000×10^{-2}
(40) $Q_5 + SO_2 = 1.400\,Q_5 + 0.3000\,Q_6 + 5.3 \times 10^{-5}\,AERS + 9.9995 \times 10^{-1}\,SO_2$	2.000×10^{-2}
(41) $Q_6 + SO_2 = 1.400\,Q_6 + 0.3000\,Q_7 + 5.3 \times 10^{-5}\,AERS + 9.9995 \times 10^{-1}\,SO_2$	2.000×10^{-2}
(42) $Q_7 + SO_2 = 1.400\,Q_7 + 5.3 \times 10^{-5}\,AERS + 9.9995 \times 10^{-1}\,SO_2$	2.000×10^{-2}
(43) $SO_2 + OH = 1.3 \times 10^{4}\,Q_1 +$ $AERS + SO_2 + OH$	$1.32 \times 10^{3}\gamma$

* Relative humidity = 80%; rate coefficient for SO_2 heterogeneous oxidation = 3×10^{-4} min^{-1}.

These kinetic equations can be matched with (6) to provide the rate parameter and stoichiometric coefficients listed in Table 3. To provide consistency among the units, the concentrations of SA and AERS in these interactions are equal to the concentrations in ppm multiplied by 1 $\mu m^3\,cm^{-3}\,ppm^{-1}$. The species SA appears on both sides of these interactions. It appears on the left side since the rate of H_2SO_4 condensation is proportional to the H_2SO_4 gas phase concentration; and it appears on the right side of the interaction so that the mass of SA removed by condensation is satisfied.

Similarly, interactions (36)–(42) represent the growth by condensation resulting from aerosol phase-reaction:

$$Q_l + SO_2 \xrightarrow{{}^{*}k_l = {}^{*}a_l Q_l + {}^{*}b_l Q_{l+1} + {}^{*}c_l AERS + {}^{*}d_l SO_2} l = 1, \ldots, m.$$

The species SO_2 appears on both sides of these interactions so that the rate of growth by condensation is proportional to the SO_2 concentration and the mass of SO_2 removed from the gas phase is correctly calculated in the kinetic equation. By matching these kinetic equations with the sectional Equation (9), we obtain the parameters listed in Table 3.

The formation of new aerosols is represented by interaction(43):

$$SO_2 + OH \xrightarrow{{}^{*}k_1 = {}^{*}a_1 Q_1} - SA + AERS + SO_2 + OH.$$

The rate is proportional to the formation rate of H_2SO_4 that occurs by homogeneous oxidation of SO_2 with OH, and is determined from monomer balance theory (see section 2.1). This interaction provides the formation of new particles, Q_1, and sulfate, AERS, as well as the depletion of H_2SO_4, SA. It does not affect

Table 3. Sectional interaction scheme: rate parameters and stoichiometric coefficients

(a) *Coagulation interactions*

$l = 1, \ldots, m$ $\quad i = l$ $\quad {}^{c}k_{i,l} = 1/2\,{}^{r}\overline{\beta}_{i,l}$ $\quad (\mu m^{-3}\,cm^{3}\,min^{-1})$

$l = 1, \ldots, m$ $\quad i = 1, \ldots, l-1$ $\quad {}^{c}k_{i,l} = {}^{r}\overline{\beta}_{i,l}$ $\quad (\mu m^{-3}\,cm^{3}\,min^{-1})$

$l = 2, \ldots, m$ $\quad i = 1, \ldots, l-1$ $\quad {}^{c}a_{i,l} = 1 - \dfrac{{}^{b}\overline{\beta}_{i,l}}{{}^{c}k_{i,l}}$

$l = 1, \ldots, m-1$ $\quad i = 1, \ldots, l$ $\quad {}^{c}b_{i,l} = \dfrac{{}^{a}\overline{\beta}_{i,l}}{{}^{c}k_{i,l}}.$

(b) *Diffusion-limited condensation interactions*

$$l = 1, \ldots, m \qquad {}^{d}k_{l} = \frac{1}{[SA]}\left[(1+\delta)\,{}^{c}\overline{\phi}_{l} + {}^{b}\overline{\phi}_{l}\right] \quad (ppm^{-1}\,min^{-1})$$

$$l = 1, \ldots, m \qquad {}^{d}a_{l} = \frac{(2+\delta)\,{}^{c}\overline{\phi}_{l}}{(1+\delta)\,{}^{c}\overline{\phi}_{l} + {}^{b}\overline{\phi}_{l}}$$

$$l = 1, \ldots, m-1 \qquad {}^{d}b_{l} = \frac{{}^{b}\overline{\phi}_{l}}{(1+\delta)\,{}^{c}\overline{\phi}_{l} + {}^{b}\overline{\phi}_{l}}$$

$$l = 1, \ldots, m \qquad {}^{d}c_{l} = \frac{\delta\,{}^{c}\overline{\phi}_{l}}{(1+\delta)\,{}^{c}\overline{\phi}_{l} + {}^{b}\overline{\phi}_{l}}$$

$$l = 1, \ldots, m \qquad {}^{d}d_{l} = \frac{{}^{c}\overline{\phi}_{l} + {}^{b}\overline{\phi}_{l}}{(1+\delta)\,{}^{c}\overline{\phi}_{l} + {}^{b}\overline{\phi}_{l}}.$$

(c) *Reaction-limited condensation interactions*

$$l = 1, \ldots, m \qquad {}^{r}k_{l} = \frac{1}{[SO_2]}\left[(1+\delta)\,{}^{c}\overline{\psi}_{l} + {}^{b}\overline{\psi}_{l}\right] \quad (ppm^{-1}\,min^{-1}),$$

$$l = 1, \ldots, m \qquad {}^{r}a_{l} = \frac{(2+\delta)\,{}^{c}\overline{\psi}_{l}}{(1+\delta)\,{}^{c}\overline{\psi}_{l} + {}^{b}\overline{\psi}_{l}}$$

$$l = 1, \ldots, m-1 \qquad {}^{r}b_{l} = \frac{{}^{b}\overline{\psi}_{l}}{(1+\delta)\,{}^{c}\overline{\psi}_{l} + {}^{b}\overline{\psi}_{l}}$$

$$l = 1, \ldots, m \qquad {}^{r}c_{l} = \frac{\delta\,{}^{c}\overline{\psi}_{l}}{(1+\delta)\,{}^{c}\overline{\psi}_{l} + {}^{b}\overline{\psi}_{l}}$$

$$l = 1, \ldots, m \qquad {}^{r}d_{l} = \frac{{}^{c}\overline{\psi}_{l} + {}^{b}\overline{\psi}_{l}}{(1+\delta)\,{}^{c}\overline{\psi}_{l} + {}^{b}\overline{\psi}_{l}}.$$

(d) *New-particle formation interaction*

$l = 1$ $\quad {}^{n}k_{1} = k_{10}\gamma \quad (ppm^{-1}\,min^{-1})$

$${}^{n}a_{1} = \frac{\varepsilon}{\delta}$$

Note: $\varepsilon = 1\,\mu m^{3}\,cm^{-3}\,ppm^{-1}$,

$$\delta = \frac{2.46 \times 10^{10}\ ppm\ mole^{-1}\,cm^{3} \times 10^{-12}\,\mu m^{-3}\,cm^{3}\,\varepsilon}{v'\left(\dfrac{P}{1\ atm}\right)},$$

where v' is the monomer volume in $cm^{3}\,mole^{-1}$ and P is the ambient pressure in atm.

the changes in the concentrations of SO_2 and OH that are taken into account in the gas phase kinetic mechanism.

Additional processes such as primary emissions or first-order removal processes can also be easily included in this scheme. The kinetic equations of the sectional interaction scheme for the aerosol sectional populations Q_l, $l = 1, \ldots, m$ are identical to Equation

(4); and the gas-to-particle conversion processes for gaseous H_2SO_4 and aerosol sulfate satisfy mass conservation.

2.3. *Evaluation of the aerosol dynamics model*

A smog chamber experiment of McMurry (1977) has been simulated that involves the formation and growth of an aerosol population resulting from the homogeneous oxidation of SO_2 and that is suitable for the evaluation of a sulfate aerosol model.

The oxidation rate of SO_2 for this simulation was 4.84×10^{-7} mol cm^{-3} s^{-1}, the initial concentration of SO_2 was 81 ppb, and the relative humidity was 34%. The experimental data at the initial time, and after 20 min, are shown in Fig. 1, in which a continuous-number size distribution has been fitted to the data points. The initial size distribution was set into a sectional form for the aerosol model.

The number of sections that will be used to represent the aerosol distribution for the simulation should provide reasonable accuracy using the minimum number of equations. The smog chamber simulation was carried out using both 7 and 14 sections to cover the aerosol diameter range from 0.01 to 2.15 μm. When coagulation only was simulated, the 7- and 14-section models agreed within 1% for all aerosol sizes. Larger differences were observed when gas-to-particle formation was included because diffusion-limited condensation is a function of aerosol diameter; therefore, the sectionalization of the distribution has a direct effect on the accuracy of the method.

Similarly, new-particle formation, which occurs in the lowest section of the model, will affect a different aerosol size range according to the section sizes. For aerosol diameters above 0.0215 μm, the 7- and 14-section models agreed within 6%. As a result of new-particle formation, the agreement for the lowest section was only within 45%. The results presented in this section were obtained with the 14-section model. It seems appropriate to use such a sectional resolution for aerosol systems with high gas-to-particle conversion rates such as smog chamber experiments. In the atmosphere, gas-to-particle conversion rates are considerably lower; thus, as shown in the next section, the 7-section model is sufficiently accurate.

Aerosol losses to the walls of the smog chamber and in the sampling lines were taken into account in the simulations according to the measurements of particle losses performed by McMurry (1977). For each aerosol section, loss of aerosol to the walls was represented by a first-order loss term. The initial aerosol volume concentrations used in the simulations were calculated from the experimental data at the initial time by correcting for particle losses in the sampling system. Similarly, the model predictions were corrected for sampling losses and, therefore, can be compared directly with the experimental data.

In this simulation, H_2SO_4 was considered to be the condensing species. Model predictions and experimental data obtained after 20 min are shown in Fig. 1. The total aerosol volume rate of change is 1.25×10^{-14} cm^3 cm^{-3} s^{-1}, which shows good agreement with the measured value of 1.17×10^{-14} cm^3 cm^{-3} s^{-1} (McMurry and Friedlander, 1979). The model results show a shift in the peak of small-particle concentrations from 0.025 to 0.04 μm and an increase in the aerosol volume as a result of diffusion-limited condensation occurring below 0.3 μm. At 20 min, the model shows two peaks in the aerosol distribution—0.04 and 0.12 μm—which do not appear as clearly in the experimental data. It should be noted, however, that simulations carried out for the same experiment

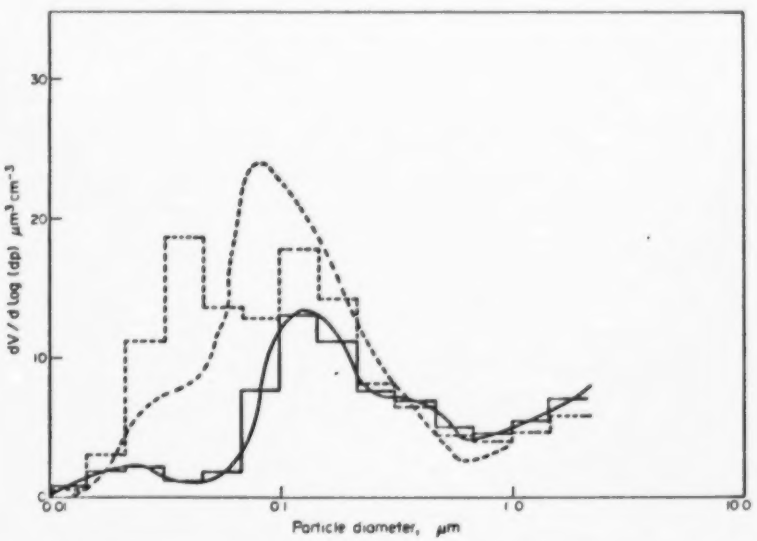

Fig. 1. Comparison of model predictions with smog chamber experimental data—experiment P. 17 (McMurry, 1977)——, initial conditions; - - -, reaction time of 20 min.

with the discrete-continuous dynamic equation also produced two distinct peaks at 0.04 and 0.14 μm (Gelbard and Seinfeld, 1979). A possible source of uncertainty in these simulations is the treatment of new-particle formation. In this model, it is assumed that cluster concentrations have reached steady state, though this might not be the case for short reaction times.

In general, there appears to be good agreement between model predictions and experimental data considering uncertainties in the measurements and the assumptions involved in the model.

3. DESCRIPTION OF THE AEROSOL PLUME MODEL

The aerosol plume model consists of three distinct components: (1) a plume model that describes advective transport, turbulent diffusion, emissions and deposition on the ground of gaseous species and aerosols; (2) a gas-phase chemistry model and (3) an aerosol model discussed in the previous section.

The Reactive Plume Model is used to describe plume dynamics. This Lagrangian model assumes a Gaussian distribution of the plume; its atmospheric dispersion coefficients are computed from Pasquill–Gifford curves or evaluated from atmospheric measurements. The plume cross-section is divided into six contiguous, well-mixed cells that expand as the plume is dispersed.

The plume is assumed to be vertically well-mixed; therefore, the model is applied best at downwind distances far from the source where vertical concentration distributions present a nearly flat profile. The model takes into account interactions between the plume and the ambient air for gaseous species as well as for aerosols. The deposition of gases and aerosols occurs when the plume contacts the ground. The development and applications of the Reactive Plume Model have been presented in detail elsewhere (Stewart and Liu, 1981).

Gas-phase chemistry is modeled with the Carbon-Bond Mechanism (Whitten *et al.*, 1980). This chemical mechanism, which has been extensively validated with smog chamber experiments, describes the chemistry of nitrogen oxides, O_3, hydrocarbons, CO and SO_2. It was developed primarily to model polluted urban atmospheres; several additional reactions have been introduced to make the mechanism suitable for clean air and plume chemistry.

In an atmosphere in which hydrocarbon concentrations are low, OH radical production results also from O_3 photolysis. This photolysis produces singlet oxygen atoms, which then react with water vapor:

$$O_3 \xrightarrow{h\nu} O(^3P) + O_2, \qquad k_1,$$

$$O_3 \xrightarrow{h\nu} O(^1D) + O_2, \qquad k_2,$$

$$O(^1D) + M \rightarrow O(^3P) + M,$$

$$k_3 = 4.45 \times 10^4\ \text{ppm}^{-1}\,\text{min}^{-1},$$

$$O(^1D) + H_2O \rightarrow 2OH,$$

$$k_4 = 3.4 \times 10^5\ \text{ppm}^{-1}\,\text{min}^{-1},$$

where k_1 and k_2 are photolysis rate parameters that depend on the solar zenith angle (Bahe *et al.*, 1979; Demerjian *et al.* 1980). These reactions can be combined because the photolysis reactions are rate-limiting:

$$O_3 \xrightarrow{h\nu} \alpha\,OH + \beta\,O(^3P), \quad k_5,$$

where

$$k_5 = k_1 + k_2,$$

$$\alpha = \frac{2k_4[H_2O]}{k_3[M] + k_4[H_2O]} \cdot \frac{k_2}{k_5},$$

$$\beta = \frac{k_1}{k_5} + \frac{k_3[M]}{k_3[M] + k_4[H_2O]} \cdot \frac{k_2}{k_5}.$$

In a clean atmosphere, OH radicals are removed by reaction with CO and CH_4. The latter reaction is not included in the original Carbon-Bond Mechanism because of the low reactivity of CH_4 compared with other hydrocarbons. Since this CH_4 reaction can be important in a clean-air atmosphere, the following reaction was introduced into the gas-phase chemistry mechanism:

$$CH_4 + OH \rightarrow CH_3 + H_2O,$$

$$k_6 = 11.6\ \text{ppm}^{-1}\,\text{min}^{-1}.$$

The chemistry of HNO_2 and H_2O_2 is not considered in the Carbon-Bond Mechanism because it does not have an important effect on the kinetics of photochemical smog. Variational sensitivity studies of a photochemical smog kinetic mechanism have confirmed that H_2O_2 could be discarded from the mechanism without noticeably affecting the concentrations of other species (Carr and Seigneur, 1979). The chemistry of HNO_2, however, is slightly more important; the following three reactions were introduced in the kinetic mechanism to describe HNO_2 chemistry.

$$NO + OH \rightarrow HNO_2$$

$$k_7 = 1.4 \times 10^4\ \text{ppm}^{-1}\,\text{min}^{-1}$$

$$HNO_2 \xrightarrow{h\nu} NO + OH$$

$$k_8 = 0.19\,k_{NO_2}$$

$$NO_2 + HO_2 \rightarrow HNO_2 + O_2$$

$$k_9 = 20\ \text{ppm}^{-1}\,\text{min}^{-1},$$

where k_{NO_2} is the photolysis rate of NO_2. In the simulations presented next, concentrations of OH radicals in the plume were about 5% lower when HNO_2 chemistry was considered.

In the Carbon-Bond Mechanism, homogeneous oxidation of SO_2 occurs through reaction with OH radicals. Oxidation of SO_2 can also occur through reaction with other radicals such as HO_2 and CH_3O_2; however, these oxidation processes are thought to be less important (G. Z. Whitten, private communication

1979; Atkinson and Lloyd, 1980) and are consequently neglected. Thus, H_2SO_4 is produced from the following reactions:

$$SO_2 + OH \xrightarrow{O_2} HSO_3, \quad k_{10} = 1.32 \times 10^3 \text{ ppm}^{-1} \text{ min}^{-1},$$

$$HSO_3 + NO \rightarrow HSO_4 + NO_2, \quad k_{11} = 8 \times 10^2 \text{ ppm}^{-1} \text{ min}^{-1},$$

$$HSO_4 + NO_2 \rightarrow H_2SO_4 + HNO_3, \quad k_{12} = 10^4 \text{ ppm}^{-1} \text{ min}^{-1}.$$

Sulfuric acid is then removed from the gas phase by nucleation with water vapor or ammonia and by condensation on existing aerosols. As a result, H_2SO_4 and SO_2 characterize the gas-to-particle conversion processes that link the gas-phase chemistry mechanism to the aerosol model. The gas-phase chemical mechanism consists of 73 reactions among 36 species.

The aerosol model is introduced into the plume model by means of the aerosol sectional scheme that was presented earlier. The complete chemistry-aerosol mechanism involves a total of 116 chemical reactions and sectional interactions among 36 chemical species and seven aerosol sectional populations, or 207 reactions and interactions if the aerosol module comprises 14 sectional populations.

4. COMPARISON OF MEASURED AND PREDICTED PLUME CONCENTRATIONS

In this section, we discuss the aerosol plume model simulation of the evolution of gaseous and aerosol concentrations in the plume of the Navajo generating station near Page, Arizona. The model results are compared with airborne measurements obtained during the VISTTA (Visibility Impairment due to Sulfur Transformation and Transport in the Atmosphere) program.

One goal of the VISTTA program was the development of a large data base that could be used for the evaluation of plume visibility models. This extensive data base includes coordinated measurements of power plant emissions, meteorological conditions, and background and plume concentrations of trace gas and aerosols, in addition to visibility measurements. Since secondary aerosol formation was observed in the plume of the Navajo generating station on several days during the VISTTA program (Richards *et al.*, 1981; Wilson and McMurry, 1981), the VISTTA data base appeared suitable for the application of the aerosol plume model.

Four days—13 July and 5, 9 and 13 December 1979—were selected for the model simulations. On these days, the MRI (Meteorology Research, Incorporated) aircraft performed 1-h orbits in the plume at several downwind distances and a 1-h orbit outside of the plume to obtain background concentrations. The background aerosol concentrations used in the following simulations are shown in Table 4. Since no information was available for plume dispersion characteristics, vertical dispersion was deduced from the Pasquill–Gifford dispersion curves, and horizontal dispersion was chosen so that predicted and measured concentrations of SO_2 would be in good agreement. Background and plume concentrations of O_3, NO, NO_2, SO_2, HNO_3, SO_4^{2-}, and aerosol distributions were obtained from aircraft measurements (L. W. Richards, private communication; Richards *et al.*, 1981). Aerosol concentration measurements were obtained with an electrical aerosol analyzer and optical particle counters. To facilitate the comparison of measurements and predictions, the measured aerosol size distributions presented next were sectionalized according to the model sectional representation. It should be noted that aerosol volume distributions and sulfate concentrations were measured independently. Richards *et al.* (1981) showed that uncertainties in the measurements lead to discrepancies between the measured secondary aerosol volume and ammonium sulfate volume. In the comparison of the model predictions with the measurements, both aerosol volume distributions and sulfate concentrations will be presented. Hydrocarbon concentrations were inferred from ground-level measurements (Sheppard *et al.*, 1980); no aldehyde measurements were available and an initial ambient concentration of 2 ppb was assumed. Emission rates of NO_x and SO_2 were obtained from stack measurements; particulate emissions were deduced from near-stack airborne measurements (Richards *et al.*, 1981). The size distributions of primary aerosols used in the simulation are those presented by Richards *et al.* (1981) in their Figs 2 (13 July case study) and 3 (December case studies).

The 7- and 14-section aerosol models were used to simulate secondary aerosol formation in a plume for

Table 4. Background aerosol concentrations used in the case studies

Case study	Aerosol volume concentration ($\mu m^3 cm^{-3}$) Q_1	Q_2	Q_3	Q_4	Q_5	Q_6	Q_7
13 July 1979	2.80×10^{-3}	1.54×10^{-2}	9.5×10^{-2}	5.45×10^{-1}	2.22×10^{-1}	3.93×10^{-2}	1.15×10^{-1}
5 December 1979	7.53×10^{-3}	8.50×10^{-3}	1.80×10^{-2}	9.43×10^{-2}	8.67×10^{-2}	6.23×10^{-2}	4.00×10^{-1}
9 December 1979	8.21×10^{-3}	2.85×10^{-2}	1.40×10^{-1}	4.56×10^{-1}	2.05×10^{-1}	9.19×10^{-2}	5.70×10^{-1}
13 December 1979	4.97×10^{-3}	3.70×10^{-3}	2.54×10^{-2}	1.36×10^{-1}	1.13×10^{-1}	8.70×10^{-2}	6.47×10^{-2}

the first case study of 13 July 1979. The models agreed within 3% after 260 min of simulation, which suggests that the 7-section model is sufficient for modeling aerosol dynamics in power plant plumes. This model was used in the following plume simulations.

Richards *et al.* (1981) showed that ammonia concentrations were high enough to neutralize the H_2SO_4 formed in the plume of the Navajo generating station. Since relative humidity was low—below 70%—for the days considered in these simulations, it was assumed that aerosols consisted of solid ammonium sulfate. The deposition velocities chosen for gases and aerosols were 0.8 and 0.1 cm s^{-1}, respectively. These are characteristic values for an arid terrain (Husar *et al.*, 1978). Plume touchdown distances were calculated according to plume vertical dispersion and terrain elevation and ranged from 30 to 40 km.

4.1. *Case study*—13 *July* 1979

The best measurements of the June–July 1979 VISTTA field program were obtained on 13 July 1979. The MRI aircraft performed two orbits at 58 and 88 km downwind of the power plant during sampling periods that extended from 0810 to 0910 and 1004 to 1104 MST, respectively. The wind speed at plume height varied from 6.3 to 3.5 m s^{-1}. According to these wind velocity measurements, a puff released from the stacks at 0605 MST corresponded to the two sampling periods considered. Relative humidity was only 16% on that day.

Predicted and measured concentrations of several chemical species are presented in Table 5. Predicted concentrations are averaged across the six plume cells. Predicted NO_x concentrations are larger than the measured concentrations; this is probably the result of uncertainties in the emission rates since day-specific data were not available and average emission rates had to be used. The rate of NO_2 formation is well predicted by the model—the NO_2/NO_x ratio is 0.49 and 0.68 at 58 and 88 km, respectively, which compares well with the measured values of 0.47 and 0.78. Sulfate formation is well predicted at 58 km, but is underestimated at 88 km. Nitric acid formation is underpredicted at both downwind distances.

Predicted and measured aerosol volume distributions are shown in Figs 2 and 3 for distances of 58 and 88 km, respectively. Predicted concentrations are averaged across the six plume cells. The aerosol concentrations shown in these figures correspond to plume concentrations above background levels. In the early morning, OH radical concentrations are low and the plume is fairly stable so that little SO_2 oxidation takes place. Later in the day, mixing of the plume with the ambient air and higher OH concentrations lead to larger sulfate formation rates. This is evident in the aerosol concentration measurements; at 58 km plume excess concentrations are low and most sulfate formation appears farther downwind.

It is interesting to note that secondary aerosol formation occurs mainly below 0.1 μm. The model

Table 5. Comparison of measured and predicted plume concentrations

	13 July 1979				5 December 1979				9 December 1979		13 December 1979	
	58 km downwind		88 km downwind		33 km downwind		80 km downwind		30 km downwind		25 km downwind	
Chemical species	Measured	Predicted	Measured	Predicted	Measured	Predicted	Measured	Predicted	Measured	Predicted	Measured	Predicted
SO_2 (ppm)	0.079	0.078	0.011	0.011	0.092	0.092	0.034	0.034	0.215	0.215	0.286	0.285
NO (ppm)	0.023	0.035	0.002	0.004	0.040	0.070	0.010	0.015	0.108	0.107	0.112	0.103
NO_2 (ppm)	0.021	0.034	0.007	0.008	0.022	0.033	0.025	0.024	0.027	0.044	0.033	0.082
O_3 (ppm)	0.041	0.021	0.060	0.044	0.017	0.008	0.024	0.014	0.015	0.007	0.010	0.010
SO_4^{2-} (μg m^{-3})*	0.23	0.19	0.76	0.24	0.07	0.06	—†	0.11	0.03	0.16	0.66	0.12
HNO_3 (μg m^{-3})	4.16	0.95	5.56	2.29	0.79	0.28	0.86	0.78	3.02	0.48	1.42	0.54

* Plume excess concentration.
† No plume excess measured.

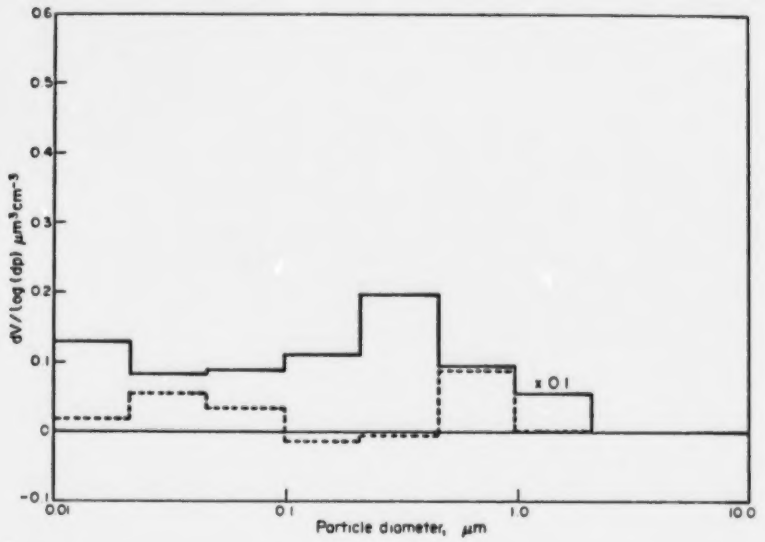

Fig. 2. Comparison of measured and predicted plume excess aerosol concentrations—13 July 1979 at 58 km downwind: - - -, measured concentration; ——, predicted concentration (aerosol concentrations in section 7 have been reduced by a factor of 10).

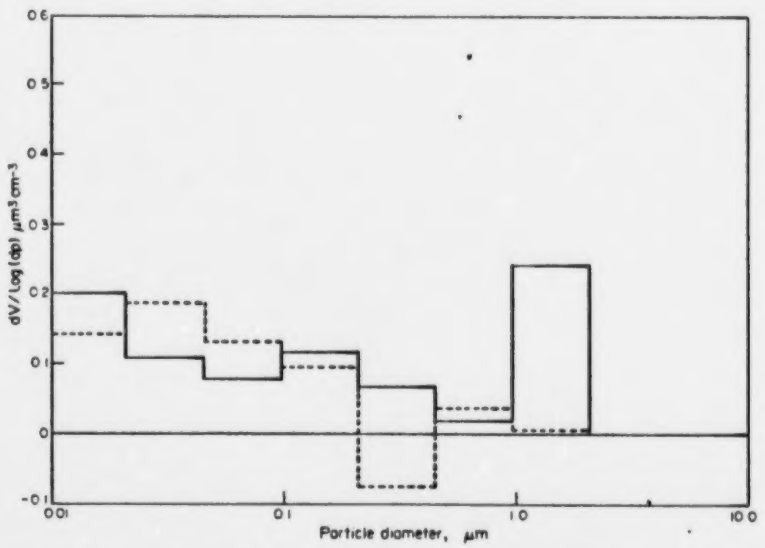

Fig. 3. Comparison of measured and predicted plume excess aerosol concentrations—13 July 1979 at 88 km downwind: - - -, measured concentration, ——, predicted concentration.

tends to overpredict aerosol formation at 58 km; however, there is good agreement below 0.1 μm, though the model predicts a peak concentration at a lower size than is measured. Predicted plume excess aerosol concentrations above 0.1 μm are mainly a result of primary aerosols. The model overpredictions are caused by uncertainties in the emission rates of aerosols. Emissions were determined from measurements obtained on 9 July 1979 (Richards *et al.*, 1981) and large variations in particulate emission rates have been reported for the Navajo generating station (Candelaria and Palomino, 1980; Richards *et al.*, 1981). This variation is particularly apparent for the largest aerosol section ($1 < d_p < 2.15$ μm).

It should also be noted that there are some uncertainties in the aerosol measurements when plume excess concentrations are of a value comparable to variations in the background concentrations. For instance, this condition appears at 88 km for section 5 ($0.215 < d_p < 0.46$ μm) where the measurements show

negative plume excess concentrations. Richards *et al.* (1981) suggested that model calculations could be used to obtain aerosol concentrations in cases for which measurement uncertainties exceed plume excess aerosol levels if good agreement could be obtained between model predictions and measurements for the aerosol size of higher plume excess concentrations.

Plume cross-section profiles predicted at 88 km are presented in Fig. 4 for the aerosol concentrations of section 1 ($0.01 < d_p < 0.0215\ \mu m$), the ratio of new-particle formation/gas-to-particle formation rates, the H_2SO_4 production rate, and SO_2 and OH concentrations. As shown in Fig. 4a, higher aerosol concentrations are predicted at the plume center. The ratio of new-particle formation/gas-to-particle formation rates decreases from the plume edges towards the plume center. This is a result of the larger primary particulate concentrations at the plume center that scavenge condensing monomers, thus reducing the new-particle formation rate.

It is interesting to note that the rate of H_2SO_4 production is nearly constant across the plume and does not vary much with downwind distance since it is about 1.05×10^{-6} ppm min^{-1} at 58 km. This is caused by the compensating variations in OH and SO_2 concentrations as the plume mixes with ambient air.

4.2. *Case study—5 December* 1979

On 5 December 1979, the MRI aircraft performed two orbits at 33 and 80 km downwind of the power plant. According to the wind measurements aloft, a puff released at 1300 MST corresponded to the sampling periods at the two downwind distances. These sampling periods extended from 1326 to 1426 MST at 33 km, and from 1455 to 1555 MST at 80 km. The background sampling was performed from 1600 to 1700 MST. Relative humidity was about 45% and the wind speed at plume height varied from 8 to 11 $m\,s^{-1}$.

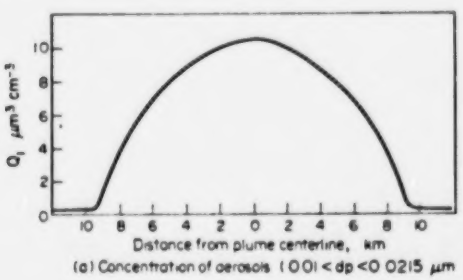

(a) Concentration of aerosols ($0.01 < dp < 0.0215\ \mu m$)

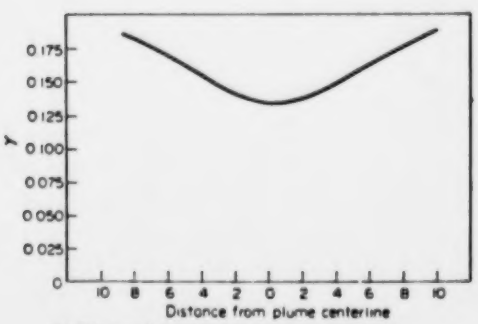

(b) Ratio γ of new-particle formation rate/gas-to particle conversion rate

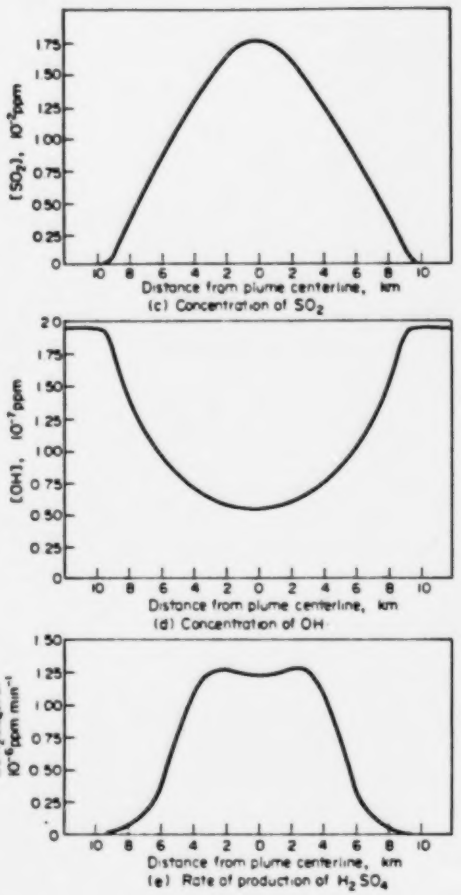
$[SO_2]$, 10^{-3}ppm
Distance from plume centerline, km
(c) Concentration of SO_2
[OH], 10^{-7}ppm
Distance from plume centerline, km
(d) Concentration of OH
$d[H_2SO_4]/dt$, 10^{-6}ppm min^{-1}
Distance from plume centerline, km
(e) Rate of production of H_2SO_4

Fig. 4. Plume cross-section profiles for the 13 July 1979 simulation at 88 km downwind.

Predicted and measured concentrations of several chemical species are shown in Table 5 for the 33 and 80 km downwind distances. Larger concentrations of NO and NO_2 are predicted downwind at 33 km compared with measured concentrations. These differences probably arise, in part, from uncertainties in the NO_x emission rates. Accordingly, the predicted O_3 concentration is lower than the measured concentration because the larger NO_x plume concentrations induce a larger consumption of O_3 by NO. The NO_2 and O_3 concentrations are in good agreement at 80 km downwind. The predicted NO_2/NO_x ratio is 0.35 and 0.71 at 33 and 80 km, respectively, which is in good agreement with the measured values of 0.32 and 0.61.

Predicted HNO_3 concentrations compare well with the measurements at 80 km, but are underestimated at 33 km. Sulfate concentrations show good agreement

between predicted and measured values at 33 km; however, the predicted increase in sulfate formation at 80 km was not apparent in the measurements, which were within the range of variations in background measurements. Less sulfate formation was observed and predicted for this day than for the 13 July 1979 case study. This difference is a result of lower OH concentrations as well as of more stable meteorological conditions that limit mixing of plume SO_2 with background OH for the December case.

Plume excess aerosol distributions are shown in Figs 5 and 6 for the 33 and 80 km downwind distances, respectively. At 33 km downwind, good agreement was observed between predicted values and measurements. The agreement is particularly good for aerosols of diameters $< 0.1\ \mu m$; variations in background values

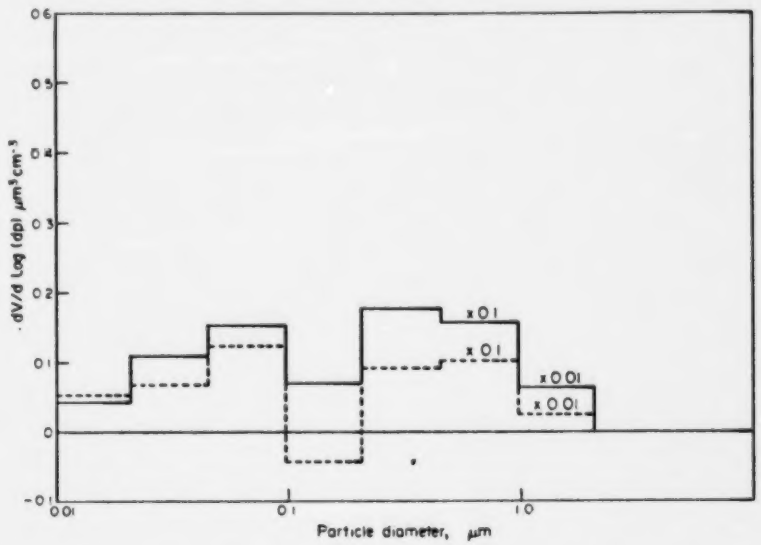

Fig. 5. Comparison of measured and predicted plume excess aerosol concentrations—5 December 1979 at 33 km downwind: – – –, measured concentration; ——, predicted concentration (aerosol concentrations in sections 6 and 7 have been reduced by factors of 10 and 100, respectively).

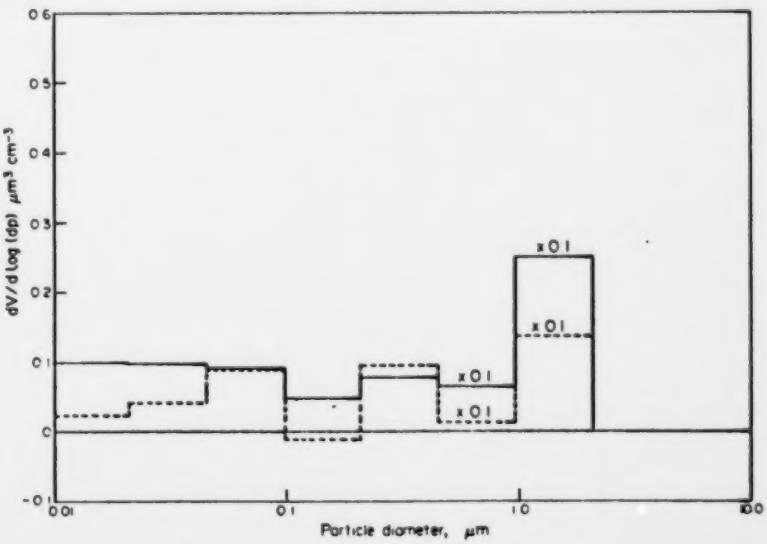

Fig. 6. Comparison of measured and predicted plume excess aerosol concentrations—5 December 1979 at 80 km downwind: – – –, measured concentration; ——, predicted concentration (aerosol concentrations in sections 6 and 7 have been reduced by a factor of 10).

make the comparison for particles above 0.1 μm more difficult. At 80 km downwind, the model overpredicts aerosol concentrations in the two lowest sections. In general, model predictions compare well with the measurements and are within measurement uncertainties for the other sections (above 0.46 μm).

Most secondary aerosol formation occurs below 0.1 μm, whereas plume excess aerosol concentrations above 0.1 μm are mainly caused by primary aerosols. This is evident when aerosol concentrations at 33 and 80 km are compared, since the decrease in aerosol volume above 0.1 μm is greater than the decrease in aerosol volume below 0.1 μm as the plume travels downwind. This decrease is caused by slower sulfate formation on this day, which does not compensate plume dilution, than on 13 July. The peak in the aerosol volume distribution in section 3 ($0.046 < d_p < 0.1\ \mu$m) is well predicted by the model at 33 km. Further downwind, the model overpredicts new-particle formation, which leads to predicted aerosol concentrations in the $0.1 - 0.1\ \mu$m range and predicted sulfate concentrations that are larger than the measured values.

4.3. *Case study—9 December* 1979

The MRI aircraft performed several orbits on 9 December 1979, and we consider here measurements obtained at 30 km downwind. Low wind speeds—from 3.4 to 4.5 m s^{-1} at plume height—were observed on that day. Under these conditions, a puff released at the stacks at 0820 MST would reach the measurement location at 1025 MST. This period of time corresponds to the sampling period, which extended from 0955 to 1055 MST. The background sampling was carried out between 1227 and 1327 MST; relative humidity was about 70%.

Predicted and measured aerosol concentrations above background levels are shown in Fig. 7. The model predicts a peak in the aerosol volume distribution in section 3 ($0.046 < d_p < 0.1\ \mu$m), whereas measurements show a peak of slightly larger particles at about 0.2 μm. The agreement for particles above 0.5 μm is very good, which suggests that primary particulate emission rates correspond well to the actual values.

The overprediction of secondary aerosol formation could be the result of an overestimation of plume mixing with the ambient air because a fairly stable plume was observed on that day. Since the model does not provide vertical resolution of plume concentration, this overestimation of plume mixing could lead to overestimation of near-source conversion rates of NO to NO_2, SO_2 to sulfate, and NO_2 to HNO_3. Table 5 shows that the model overpredicts NO_2 and sulfate formation. Nitric acid formation however is underpredicted by the model.

Another possible source of uncertainty is found in the background hydrocarbon concentrations. The only available hydrocarbon measurements were obtained in the summer of 1979. The OH radical concentrations are sensitive to hydrocarbon levels; lower background hydrocarbon concentrations would lead to lower predicted sulfate formation.

More secondary aerosol formation is predicted on 9 December than on 5 December. This is caused, in part, by the lower wind speeds observed on 9 December. Aerosol concentration profiles at 10 and 30 km downwind are shown in Fig. 8, for the lowest section, i.e.

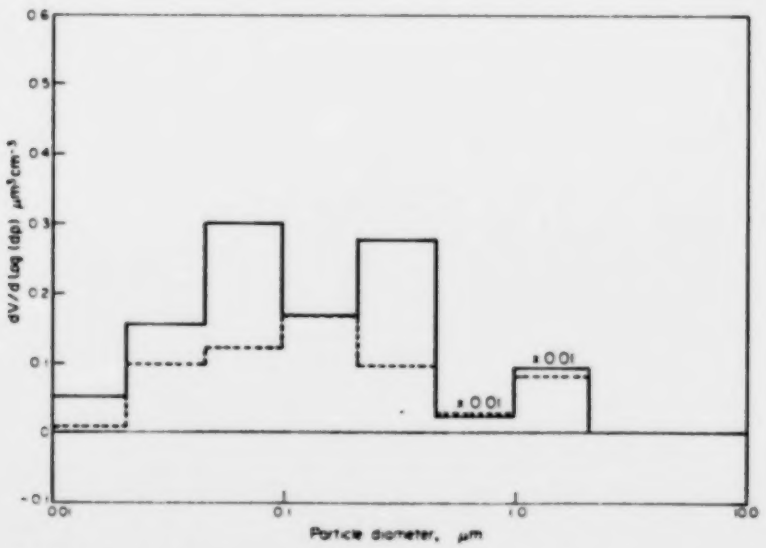

Fig. 7. Comparison of measured and predicted plume excess aerosol concentrations—9 December 1979 at 30 km downwind: - - -, measured concentration; ——, predicted concentration (aerosol concentrations in sections 6 and 7 have been reduced by a factor of 100).

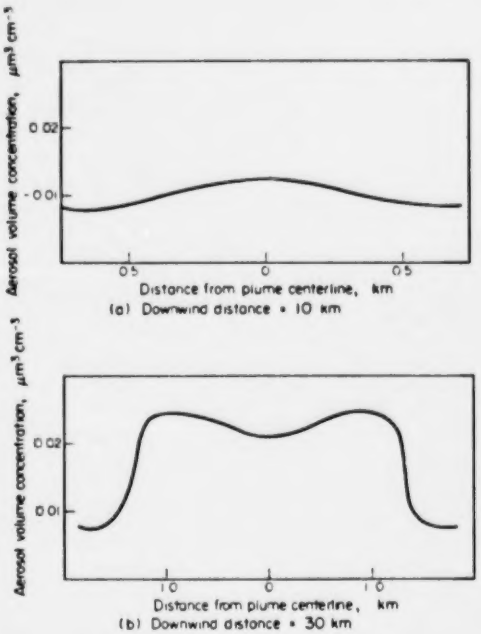

Fig. 8. Plume cross-section profiles, aerosol concentrations, section 1 ($0.01 < d_p < 0.0215\,\mu$m), for the 9 December 1979 simulation.

$0.01 < d_p < 0.0215\,\mu$m. It appears that at 30 km, the maximum aerosol concentration occurs at the plume edges. The rate of new-particle formation decreases as the total aerosol surface area increases; thus, lower rates of new-particle formation are observed at the plume center. Moreover, the coagulation rates of small particles will be lower at the plume edges because of lower concentrations of particles of a larger size. The combination of these two effects leads to an increase in small-particle concentrations that overcomes the effect of plume mixing with the ambient air. Higher concentrations of small particles at the plume edges were not obtained for the 13 July case because plume dilution was more important and entrainment of low background concentrations of aerosols decreased plume concentrations at the edges.

4.4. *Case study*—13 *December* 1979

The MRI aircraft performed several orbits on 13 December 1979. Low wind speeds were observed on that day and good data on secondary sulfate formation were obtained. We consider here measurements obtained during a 1-h sampling orbit that was performed at 25 km downwind between 1002 and 1102 MST. A wind speed of $2\,m\,s^{-1}$ was used in the simulation.

Chemical species concentrations are presented in Table 5. The rate of conversion of NO to NO_2 is overpredicted by the model—0.44 vs a measured value of 0.23 for the NO_2/NO_x ratio. The HNO_2 and sulfate formation rates, however, are underestimated by the model. It is likely that the stable atmosphere and low wind speeds make the mixing of the plume with the ambient air difficult to model.

Aerosol volume distributions are shown in Fig. 9. There is a very good agreement between predicted and measured values below 0.46 μm. The peak volume distribution occurs in the third section ($0.046 < d_p < 0.1\,\mu$m) for both the predictions and the measured data. For large aerosol particle sizes, measured aerosol

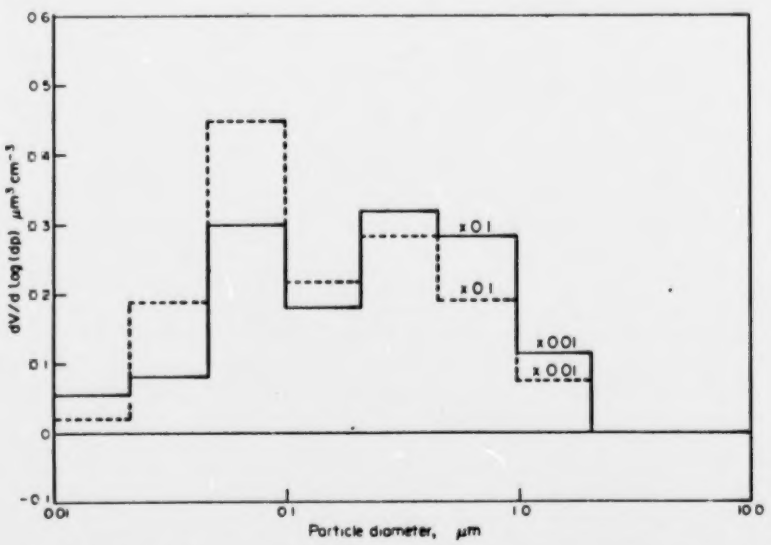

Fig. 9. Comparison of measured and predicted plume excess aerosol concentrations—13 December 1979 at 25 km downwind: ---, measured concentration; ——, predicted concentration (aerosol concentrations in sections 6 and 7 have been reduced by factors of 10 and 100, respectively).

concentrations are slightly lower than the predicted values; the differences, however, are well within the uncertainties for primary particulate emission rates.

5. SENSITIVITY STUDIES OF THE AEROSOL PLUME MODEL

The sensitivity of aerosol volume concentrations to various parameters such as meteorological conditions or emission rates is difficult to determine from atmospheric measurements or from a simple analysis of the processes involved because of complex interactions between transport processes, gas-phase reactions and aerosol dynamics in atmospheric plumes. A mathematical model can be used advantageously to theoretically investigate this sensitivity to variations in some parameters. In this section, we analyze the effect of changes in emission rates, aerosol growth law, background hydrocarbon concentrations and meteorological parameters on the evolution of the aerosol volume distribution. The excess plume aerosol volume concentrations and sulfate concentrations are listed for the base case (see section 4.1) and several sensitivity cases in Table 6 for the 13 July 1979 simulation at 88 km downwind.

5.1. *Sulfur dioxide emissions*

It is important to evaluate the effect of emission rates on aerosol formation because air quality standards must be achieved through appropriate control of the emission levels of primary pollutants. Since SO_2 is the primary pollutant in the formation and growth of aerosols in power plant and smelter plumes, we considered the sensitivity of sulfate formation to SO_2 emissions in this study by increasing the SO_2 emission rate by 50%. As shown in Table 6, the sensitivity relationship between sulfate formation and SO_2 emissions is not exactly linear; excess plume sulfate concentrations are increased by only 43%. Higher SO_2 concentrations in the plume allow a lower diffusion rate of OH radicals into the plume; consequently, the oxidation rate of SO_2 is slightly lower when the SO_2 emission rate increases. This compensating effect of OH diffusion into the plume leads to the nonlinearity of the sensitivity relationship. The largest increase in aerosol volume concentrations occurred in the 0.01–0.1 μm diameter range, and corresponds to the particle size range in which most of the sulfate is formed. The lowest variation is observed for the largest particle sizes (i.e. section 7).

5.2. *Nitrogen oxide emissions*

Nitrogen oxides, NO and NO_2, play a major role in atmospheric chemical kinetics and, consequently, their emission rates affect the formation of secondary aerosols. Emissions of nitrogen oxides were increased by 50% in this study, which resulted in a decrease in sulfate formation of 24%. Higher NO concentrations in a plume lead to lower O_3 and OH radical concentrations as more O_3 is consumed by NO and more OH

Table 6. Excess plume aerosol concentrations ΔQ_i, $i = 1, \ldots, 7$ ($\mu m^3 cm^{-3}$) and sulfate concentrations ($\mu g\ m^{-3}$) at 88 km downwind—simulation of 13 July 1979

Excess plume concentrations	Base case	SO_2 Emissions increased by 50%	NO, Emissions increased by 50%	Relative humidity 80%; acid sulfate aerosol	Heterogeneous oxidation of SO_2, $k_e = 3 \times 10^{-4}$ min^{-1}	Hydrocarbon concentrations increased by 100%	Plume width and plume depth decreased by 50%	Photolysis parameters reduced by 50%
ΔQ_1	6.60×10^{-2}	1.00×10^{-1}	4.59×10^{-2}	2.81×10^{-1}	2.82×10^{-1}	1.33×10^{-1}	8.02×10^{-2}	1.77×10^{-2}
ΔQ_2	3.47×10^{-2}	5.94×10^{-2}	2.23×10^{-2}	3.86×10^{-1}	2.67×10^{-1}	9.72×10^{-2}	4.43×10^{-2}	9.27×10^{-3}
ΔQ_3	2.55×10^{-2}	3.35×10^{-2}	2.07×10^{-2}	1.38×10^{-1}	2.33×10^{-1}	4.42×10^{-2}	3.54×10^{-2}	1.30×10^{-2}
ΔQ_4	3.85×10^{-2}	4.59×10^{-2}	3.32×10^{-2}	8.27×10^{-2}	5.44×10^{-1}	5.19×10^{-2}	4.40×10^{-2}	2.13×10^{-2}
ΔQ_5	2.17×10^{-2}	2.44×10^{-2}	1.95×10^{-2}	3.50×10^{-2}	2.93×10^{-1}	2.63×10^{-2}	4.56×10^{-2}	1.56×10^{-2}
ΔQ_6	5.75×10^{-3}	6.09×10^{-3}	5.36×10^{-3}	7.16×10^{-3}	1.26×10^{-2}	6.27×10^{-3}	1.84×10^{-2}	5.13×10^{-3}
ΔQ_7	8.00×10^{-3}	8.18×10^{-3}	7.65×10^{-3}	8.33×10^{-3}	8.44×10^{-2}	8.17×10^{-3}	2.95×10^{-1}	7.95×10^{-2}
Sulfate	0.243	0.349	0.184	0.246	0.383	0.466	0.303	0.095

radicals by NO_2. It should be noted that in the case of high hydrocarbon concentrations, higher NO concentrations could lead to more O_3 formation far downwind of the stacks. Since hydrocarbon concentrations were low in the case considered here, lower O_3 concentrations were observed in the plume. This condition leads to lower OH concentrations because OH radicals are, in part, produced from O_3 photolysis. Consequently, SO_2 oxidation rates are lower and less sulfate formation is observed. This suggests that in smelter plumes, when NO concentrations are negligible compared with SO_2 concentrations, higher SO_2 oxidation rates will be observed because O_3 and OH concentrations in the plume will be higher.

5.3. *Relative humidity*

Relative humidity can have an important effect on aerosol growth since, at low humidities, secondary aerosol will consist of solid ammonium sulfate, whereas, at humidities above 80%, ammonium sulfate will deliquesce and secondary aerosol will consist of aqueous sulfate. A simulation was carried out assuming that the secondary aerosol was acid sulfate. Ideally, it would be necessary to consider the liquid-phase chemical equilibrium of the aerosol with the NH_3 containing ambient air. However, the assumption of an acid sulfate aerosol is sufficient to provide some information on the effect of relative humidity on aerosol volume concentrations. The general effect is an increase in volume concentrations at all aerosol sizes; it is most apparent, however, for smaller aerosols, which undergo the largest aerosol growth.

5.4. *Heterogeneous oxidation of* SO_2

Heterogeneous oxidation of SO_2 can occur through catalyzed or uncatalyzed reactions (Freiberg, 1975; Penkett *et al.*, 1979). Recently, it has been estimated that up to 20% of the total oxidation rate of SO_2 in power plant plumes could be caused by heterogeneous oxidation (McMurry *et al.*, 1981). To evaluate the effect of heterogeneous oxidation on the evolution of the aerosol number distribution, a simulation was carried out with pseudo-first-order oxidation of SO_2 in the liquid phase. The rate parameter chosen was $k = 3 \times 10^{-4}\ \text{min}^{-1}$ for heterogeneous oxidation of aerosol particles below 0.46 μm. Larger aerosols consist mainly of primary aerosols and no liquid phase oxidation was considered to occur for aerosols above 0.46 μm.

Sulfate formation caused by heterogeneous oxidation decreases sharply as the plume is dispersed; it accounts for 80% of all sulfate formed at 58 km, but for only 35% at 88 km. The rate of heterogeneous oxidation of SO_2 depends on the partial pressure of SO_2 in the gas phase, which decreases as the plume moves downwind. The rate of homogeneous oxidation decreases also since it is proportional to the partial pressure of SO_2; however, it depends on the concentration of OH radicals in the plume as well. Therefore, the larger diffusion of OH radicals as the plume is dispersed induces a compensating effect (see Fig. 4) that results in a slower rate of decrease for homogeneous oxidation compared with heterogeneous oxidation. Consequently, the contribution of heterogeneous oxidation to the total oxidation rate decreases as the plume is dispersed.

Heterogeneous oxidation results in more aerosol growth, predominantly at larger sizes, because the corresponding particle diameter growth law is directly proportional to the particle diameter. In contrast, the particle diameter growth law for homogeneous oxidation is constant in the small-particle size range and is inversely proportional to the particle size for larger sizes. Lower concentrations are observed in sections 1 and 2 ($0.01 < d_p < 0.046\ \mu$m) because of the larger surface area of the accumulation mode aerosols, which leads to higher coagulation rates for smaller particles.

5.5. *Background hydrocarbon concentrations*

Background hydrocarbon concentrations were increased by a factor of two in this simulation, which produced an increase in background OH radical concentrations in the early morning. Later in the day, O_3 photolysis becomes the predominant source of OH radicals, whereas hydrocarbons act more as a sink for OH radicals through oxidation reactions. A large increase in sulfate formation—approximately 90%—is the result of the larger concentrations of OH radicals that are entrained into the plume. The model is very sensitive to background hydrocarbon concentrations, which suggests that the largest secondary aerosol formation rates will occur at power plants located near urban areas. At the Navajo generating station, sulfate formation rates will increase when, for example, the area is affected by the Southern California urban plume (Macias *et al.*, 1981).

5.6. *Atmospheric stability*

Atmospheric stability has a strong effect on plume dispersion; in this sensitivity study, the simulation was carried out using a plume width and depth reduced by 50%; the concentrations of inert species were accordingly increased by a factor of 4. Sulfate formation, however, is not very sensitive to plume dispersion since it increased by only 25%. This low variation in sulfate formation rates is caused by the compensating effect of OH diffusion into the plume when dispersion occurs. This effect appears mainly in the aerosol section below 0.2 μm, where most sulfate is formed. Sections containing larger particles show a larger increase in volume concentrations; this increase tend towards the behaviour of plume inert species as the particle size increases because aerosol concentrations at these sizes are mainly caused by primary aerosols.

5.7. *Photolysis rates*

Daytime atmospheric chemistry is largely determined by photochemical reactions such as NO_2 and O_3 photolysis. In this sensitivity study, the rates of the photochemical reactions were reduced by 50%. Nitrogen dioxide is photolyzed to NO and triplet

oxygen atoms, therefore, a decrease in the photolysis rate led to lower O_3 concentrations according to the photostationary-state relationship. Moreover, a lower photolytic decomposition rate of O_3 and aldehydes led to less OH radical production. Consequently, the conversion rate of SO_2 was reduced, and a reduction in photolysis rates of 50% induced a decrease in sulfate formation of 61%.

The dependence of secondary aerosol formation upon u.v. radiation has been observed in atmospheric plumes (e.g. Wilson and McMurry, 1981). Further investigation of this relationship using a detailed mathematical model could provide useful information for the development of simple aerosol models.

6. CONCLUSIONS

Using an aerosol dynamics model based on a sectional representation of the aerosol distribution, it was shown that a 7-section model is accurate enough for the simulation of aerosol growth in the atmosphere, however, for higher gas-to-particle conversion rates (e.g. smog chamber experiments), a more detailed resolution of the aerosol distribution is recommended. The aerosol dynamics module was evaluated with data from a smog chamber experiment. The sectional model results showed good agreement with the experimental data, though the bimodal volume distribution was not as apparent in the experimental volume distribution.

The model has been used to simulate gas-phase chemistry and the evolution of the aerosol volume distribution in the plume of the Navajo generating station on four different days, with different meteorological conditions. The rate of NO to NO_2 is well predicted by the model with the exception of the 13 December case, for which it is overpredicted. Predicted HNO_2 concentrations are lower than the measured values for all cases. The maximum oxidation rates of SO_2 are 0.5 and 0.06% per hour in July and December, respectively. The maximum measured rates were 0.8 and 0.2% h^{-1} on 13 July and 12 December, respectively (Richards *et al.*, 1981). The largest uncertainties occur for aerosol concentrations above 0.5 μm and are caused by uncertainties in the emissions rates of primary aerosols. The model reproduces well the dynamics of aerosol growth in power plant plumes, considering the uncertainties in the input data (e.g. wind speed, atmospheric stability, hydrocarbon concentrations and emission rates). In general, most secondary aerosol formation is predicted and observed to occur in the 0.01–0.1 μm particle diameter range. The largest increase in secondary aerosol formation occurs for the 13 July case study. Both model predictions and measurements show an increase in aerosol concentrations for particles in the diameter range of 0.01–0.1 μm, for distances between 58 and 88 km downwind.

Predictions for the 5 December case show a slight decrease in aerosol concentrations for diameters below 0.1 μm, at distances between 33 and 80 km. This is caused by secondary aerosol formation rates that are lower than those of 13 July. The 9 and 13 December cases were characterized by lower wind speed. The model overestimated aerosol growth for the 9 December case; very good agreement between the measured and predicted aerosol size distributions was obtained for the 13 December case.

In general, maximum concentrations of aerosols are observed at the plume centerline since background aerosols of lower concentrations are entrained at the plume edges. However, in the case of a stable plume (e.g. 9 and 13 December), for which there is less entrainment of low ambient concentrations of aerosols, maximum concentrations of aerosols from the nuclei mode are predicted at the plume edges because the rate of coagulation of these small particles with primary particles is higher in the plume center than at the plume edges.

Several studies of the sensitivity of secondary aerosol formation to emission rates, aerosol growth law, meteorological parameters and background hydrocarbon concentrations were conducted. Because of the complex interactions between turbulent diffusion processes, gas-phase chemical kinetics and aerosol dynamics, the sensitivity relationships were nonlinear. Secondary aerosol formation appeared to be fairly insensitive to plume dispersion and very sensitive to relative humidity, photolysis rates and background hydrocarbon concentrations. An increase in SO_2 emissions by 50% led to an increase of only 43% in sulfate formation; an increase in NO_2 emissions of 50% led to a decrease of 24% in sulfate formation caused in part by the scavenging of OH radicals by the higher NO_2 concentrations. The importance of heterogeneous oxidation decreases as the plume is dispersed.

The model presented here appears to provide a promising technique for the simulation of the evolution of trace gas and aerosol concentrations in atmospheric plumes, as well as for the theoretical investigation of the parameters or variables that affect secondary aerosol formation. Moreover, the sectional representation of the aerosol distribution can allow for the coupling of the aerosol dynamics module with a liquid-phase aerosol model that could provide a more detailed description of the aerosol growth laws. Further studies of aerosol dynamics in atmospheric plumes should include both the formation of sulfate aerosol by heterogeneous oxidation of SO_2 as it might occur at high relative humidity and the comparison of sulfate oxidation rates in power plant and smelter plumes.

Acknowledgements—This work was supported, in part, by the Environmental Protection Agency under Contracts 68-02-3337 (Project VISTTA, under the direction of Dr. W. E. Wilson) and 68-02-3225. Thanks are due to Prof. J. H. Seinfeld for suggesting the sectional approach to model aerosol dynamics, to F. Gelbard, R. W. Bergstrom, D. A.

Latimer and G. Z. Whitten for helpful suggestions throughout the course of this study, to L. W. Richards for providing useful information and comments concerning the VISTTA field measurements, and to A. B. Hudischewskyj for performing the model simulations. Thanks are also due to K. Pullen and C. Lawson for editorial assistance.

REFERENCES

Atkinson R. and Lloyd A. C. (1980) ERT document No. P-A040. Environmental Research and Technology, Westlake Village, California.

Bahe F. C., Marx W. N., Schurath U. and Roth E. P. (1979) Determination of the absolute photolysis rate of ozone by sunlight, $O_3 + h\nu \rightarrow O(^1D) + O_2(^1\Delta_g)$, at ground level. *Atmospheric Environment* **13**, 1515–1522.

Basset M., Gelbard F. and Seinfeld J. H. (1981) Mathematical model for multicomponent aerosol formation and growth in plumes. *Atmospheric Environment* **15**, 2395–2406.

Candelaria R. B. and Palomino G. E. (1980) Characterization of Navajo generating station emissions measured during the June–July 1979 VISTTA field program. Preprints Symp. on Plumes and Visibility: Measurements and Model Components, Grand Canyon, Arizona, 10–14 November 1980.

Carr R. W., Jr. and Seigneur C. (1979) Dynamic sensitivity analysis of chemical reaction systems. *Proc.* 178th *Am. Chem. Soc. Nat. Meeting*, Washington, DC., 9–14 September 1979.

Chu K. J. and Seinfeld J. H. (1975) Formulation and initial application of a dynamic model for urban aerosols. *Atmospheric Environment* **3**, 375–402.

Davis E. J. and Ray A. K. (1978) Submicron droplet evaporation in the continuum and noncontinuum regimes. *J. Aerosol Sci.* **9**, 411–422.

Davis D. D., Ravishankara A. R. and Fischer S. (1979) SO_2 oxidation via the hydroxyl radical: atmospheric fate of HSO_3 radicals. *Geophys. Res. Lett.* **6**, 113–116.

Demerjian K. L., Schere K. L. and Peterson J. T. (1980) Theoretical estimates of actinic (spherically integrated) flux and photolytic rate constants of atmospheric species in the lower troposphere. *Adv. Envir. Sci. Technol.* **10**, 369–460.

Eltgroth M. W. and Hobbs P. V. (1979) Evolution of particles in the plumes of coal-fired power plants—II. A numerical model and comparisons with field measurements. *Atmospheric Environment* **13**, 953–975.

Freiberg J. (1975) The mechanism of iron catalyzed oxidation of SO_2 in oxygenated solutions. *Atmospheric Environment* **9**, 661–672.

Friedlander S. K. (1977) *Smoke, Dust and Haze—Fundamentals of Aerosol Behavior*, John Wiley, New York.

Fuchs N. A. and Sutugin A. G. (1971) High dispersed aerosols. In *Topics in Current Aerosol Research* (Edited by G. M. Hidy and J. R. Brock), pp. 1–60.

Gelbard F. and Seinfeld J. H. (1979) The general dynamic equation for aerosols—theory and application to aerosol formation and growth. *J. Colloid Interface Sci.* **68**, 363–382.

Gelbard F. and Seinfeld J. H. (1980) Simulation of multicomponent aerosol dynamics. *J. Colloid Interface Sci.* **78**, 485–501.

Gelbard F., Tambour Y. and Seinfeld J. H. (1980) Sectional representation for simulating aerosol dynamics. *J. Colloid Interface Sci.* **76**, 541–556.

Gmitro J. I and Vermeulen T. (1969) Vapor–liquid equilibria for aqueous sulfuric acid. *A.I.Ch.E.Jl* **10**, 740–746.

Hobbs P. V., Hegg D. A., Eltgroth M. W. and Radke L. F. (1979) Evolution of particles in the plumes of coal-fired power plants –I. Deductions from field measurements. *Atmospheric Environment* **12**, 935–951.

Husar R. B., Lodge J. P., Jr. and Moore D. J. (1978) Sulfur in the atmosphere. *Atmospheric Environment* **12**, 7–23.

Macias E. S., Zwicker J. O. and White W. H. (1981) Regional haze case studies in the southwestern U.S.—II. Source contributions. *Atmospheric Environment* **15**, 1987–1997.

McMurry P. H. (1977) On the relationship between aerosol dynamics and the rate of gas-to-particle conversion. Ph.D. thesis, California Institute of Technology, Pasadena, California.

McMurry P. H. (1980) The dynamic behavior of photochemical aerosols. Particle Technology Laboratory Publication No. 431, University of Minnesota, Minneapolis, Minnesota.

McMurry P. H. and Friedlander S. K. (1979) New particle formation in the presence of an aerosol. *Atmospheric Environment* **13**, 1635–1651.

McMurry P. H., Rader D. J. and Stith J. L. (1981) Growth laws for secondary aerosols in power plant plumes: implications for chemical conversion mechanisms. *Atmospheric Environment* **15**, 2315–2327.

Middleton P. and Brock J. (1976) Simulation of aerosol kinetics. *J. Colloid Interface Sci.* **54**, 249–264.

Middleton P. and Kiang C. S. (1978) A kinetic aerosol model for the formation and growth of secondary sulfuric acid particles. *J. Aerosol Sci.* **9**, 359–385.

Mirabel P. and Katz J. L. (1974) Binary homogeneous nucleation as a mechanism for the formation of aerosols. *J. chem. Phys.* **60**, 1138–1144.

Penkett S. A., Jones B. M. R., Brice K. A. and Eggleton A. E. J. (1979a) The importance of atmospheric ozone and hydrogen peroxide in oxidizing sulphur dioxide in cloud and rainwater. *Atmospheric Environment* **13**, 123–138.

Penkett S. A., Jones B. M. R. and Eggleton A. E. J. (1979b) A study of SO_2 oxidation in stored rainwater samples. *Atmospheric Environment* **13**, 139–148.

Peterson T. W. and Seinfeld J. H. (1977) Mathematical model for transport, interconversion and removal of gaseous and particulate air pollutants—application to the urban plume. *Atmospheric Environment* **11**, 1171–1184.

Richards L. W., Anderson J. A., Blumenthal D. L., Brandt A. A., McDonald J. A., Waters N., Macias E. S. and Bhardwaja P. S. (1981) The chemistry aerosol physics, and optical properties of a western coal-fired power plant plume. *Atmospheric Environment* **15**, 2111–2134.

Sheih C. M. (1977) Mathematical modeling of particulate thermal coagulation and transport downstream of an urban area source. *Atmospheric Environment* **11**, 1185–1190.

Sheppard J. C., Campbell M., McMurry P. M. and Kolk G. L. (1980) Trace gas and and particle data from a remote site in northern Arizona. Unpublished results.

Sitarski M. and Seinfeld J. H. (1977) Brownian coagulation in the transition regime. *J. Colloid Interface Sci.* **61**, 261–271.

Stewart D. A. and Liu M. K. (1981) Development and application of a reactive plume model. *Atmospheric Environment* **15**, 2377–2393.

Whitby K. T., Husar R. B. and Liu B. Y. M. (1972) The aerosol size distribution of Los Angeles smog. *J. Colloid Interface Sci.* **39**, 177–204.

Whitby K. T., Clark W. E., Marple V. A., Sverdrup G. M., Sem G. J., Willeke K., Liu B. Y. M. and Pui D. Y. H. (1975) Characterization of California aerosols—I. Size distributions of freeway aerosol. *Atmospheric Environment* **9**, 463–482.

Whitten G. Z., Killus J. P. and Hogo H. (1980) Modeling of simulated photochemical smog with kinetic mechanisms EF79-129. Systems Applications, San Rafael, California.

Wilson J. C. and McMurry P. H. (1981) Aerosol formation in power plant plumes—II. Secondary aerosol formation in the Navajo power plant plume. *Atmospheric Environment* **15**, 2329–2339.

Yue G. K. and Hamill P. (1979) The homogeneous nu-

cleation rates of H_2SO_4-H_2O aerosol particles in air. *J. Aerosol Sci.* **10**, 609–614.

APPENDIX

Derivation of the sectional condensation equations

The sectional equations for gas-to-particle conversion can be derived in the following manner. First, the increase in aerosol volume of section l as a result of condensation is given by

$$\left.\frac{dQ_l}{dt}\right|_{add} = \int_{x_{l-1}}^{x_l} \phi n(x)dx, \tag{A1}$$

where $n(x)$ is the number concentration of aerosol particles between x and $x + dx$, and ϕ is the growth law. This is related to the aerosol volume in the following manner:

$$n(x) = \frac{Q_l}{v(x_l - x_{l-1})}. \tag{A2}$$

Then, the rate of volume increase can be expressed by (A3):

$$\left.\frac{dQ_l}{dt}\right|_{add} = Q_l \int_{x_{l-1}}^{x_l} \frac{\phi}{v(x_l - x_{l-1})} dx. \tag{A3}$$

The fraction of the total concentration of aerosol particles from sections l, N_l, which grows out of the section l by condensation during a time interval, Δt, is given by the following equation:

$$\Delta N_l = -N_l \frac{\Delta x|l}{x_l - x_{l-1}}, \tag{A4}$$

where $\Delta x|l$ is the growth of a particle from section l during time Δt. The flux of aerosol out of section l is then given by (A5):

$$\left.\frac{dN_l}{dt}\right|_{out} = N_l \frac{1}{(x_l - x_{l-1})} \left.\frac{dx}{dt}\right|_l. \tag{A5}$$

Let ϕ_l be the growth law resulting from condensation for section l and V_l the volume of an aerosol of size x_l.

$$\phi_l = \frac{dV_l}{dt}. \tag{A6}$$

Equation (A5) can then be rewritten in this manner for the flux of aerosol volume:

$$\left.\frac{dQ_l}{dt}\right|_{out} = Q_l \frac{1}{(x_l - x_{l-1})} \phi_l \left.\frac{dx}{dr}\right|_l \frac{(r_l + r')}{r_l}, \tag{A7}$$

where the last term accounts for the increase in volume resulting from the condensation of a monomer of volume, v'.

The flux into section l as a result of growth from section $(l-1)$ is obtained similarly:

$$\left.\frac{dQ_l}{dt}\right|_{in} = Q_{l-1} \frac{1}{x_{l-1} - x_{l-2}} \phi_{l-1} \left.\frac{dx}{dr}\right|_{l-1} \frac{(r_{l-1} + r')}{r_{l-1}}. \tag{A8}$$

The sectional equations showing aerosol growth by condensation are then given by

$$\frac{dQ_l}{dt} = \left.\frac{dQ_l}{dt}\right|_{add} + \left.\frac{dQ_l}{dt}\right|_{in} + \left.\frac{dQ_l}{dt}\right|_{out} \qquad l = 1, \ldots, m, \tag{A9}$$

which can be expressed as follows:

$$\frac{dQ_l}{dt} = {}^{a}\overline{\phi}_l Q_l + {}^{b}\overline{\phi}_{l-1} Q_{l-1} - {}^{b}\overline{\phi}_l Q_l \qquad l = 1, \ldots, m, \tag{A10}$$

where the second term on the right-hand side is not evaluated for $l = 1$. The sectional condensation coefficients, ${}^{a}\overline{\phi}_l$ and ${}^{b}\overline{\phi}_l$, which are calculated from Equation (7), are listed in Table 1.

F. Gelbard (private communication) noted that the derivation of the sectional condensation coefficients presented here leads to the same condensation equation as the approach used by Gelbard and Seinfeld (1980). The rate at which the aerosol grows out of section l is given (Gelbard and Seinfeld, 1980) by ${}^{2}\overline{G}_l Q_l$, where

$${}^{2}\overline{G}_l = \int_{f(v_l - v')}^{x_l} \frac{G(v)}{x_l - x_{l-1}} dx, \tag{A11}$$

and $G(v)$ is the rate at which molecules of size v' condense on a particle, rewritten as follows;

$${}^{2}\overline{G}_l = \int_{v_l - v'}^{v_l} \frac{\phi}{(x_l - x_{l-1})v'} \frac{dx}{dv} dv \approx \left.\frac{\phi_l}{x_l - x_{l-1}} \frac{dx}{dv}\right|_{v = v_l}. \tag{A12}$$

The rate of change of Q_l resulting from diffusion-limited condensation as expressed in Gelbard and Seinfeld (1980) is as follows:

$$\begin{aligned}\frac{dQ_l}{dt} = &\int_{x_{l-1}}^{f(v_l - v')} \frac{\phi Q_l}{v(x_l - x_{l-1})} dx - \frac{\phi_l}{(x_l - x_{l-1})} Q_l \left.\frac{dx}{dv}\right|_{v = v_l} \\ &+ \frac{\phi_{l-1}}{(x_{l-1} - x_{l-2})} Q_{l-1} \left.\frac{dx}{dv}\right|_{v = v_{l-1}} \\ &+ \int_{f(v_{l-1} - v')}^{x_{l-1}} \frac{\phi Q_{l-1}}{v(x_{l-1} - x_{l-2})} dx.\end{aligned} \tag{A13}$$

The first term can be rewritten in the following manner:

$$\int_{x_{l-1}}^{x_l} \frac{\phi Q_l}{v(x_l - x_{l-1})} dx - \int_{f(v_l - v')}^{x_l} \frac{\phi Q_l}{v(x_l - x_{l-1})} dx. \tag{A14}$$

Since $v' \ll v_l$, last integrals of Equations (A13) and (A14) can be obtained. For instance,

$$\int_{f(v_l - v')}^{x_l} \frac{\phi Q_l}{v(x_l - x_{l-1})} dx \approx \left.\frac{v' \phi_l Q_l}{v_l (x_l - x_{l-1})} \frac{dx}{dv}\right|_{v = v_l}. \tag{A15}$$

Thus, Equation (A13) becomes

$$\begin{aligned}\frac{dQ_l}{dt} = &Q_l \int_{x_{l-1}}^{x_l} \frac{\phi}{v(x_l - x_{l-1})} dx \\ &- \left.\frac{\phi_l}{(x_l - x_{l-1})} \frac{dx}{dv}\right|_{v = v_l} \cdot \frac{v_l + v'}{v_l} Q_l \\ &+ \left.\frac{\phi_{l-1}}{(x_{l-1} - x_{l-2})} \frac{dx}{dv}\right|_{v = v_{l-1}} \cdot \frac{v_{l-1} + v'}{v_{l-1}} \cdot Q_{l-1},\end{aligned} \tag{A16}$$

which is equivalent to Equation (A10).